Competition of Failure Modes in an Additively Manufactured Disk Superalloy

Timothy P. Gabb and Chantal K. Sudbrack
Glenn Research Center, Cleveland, Ohio

Michael M. Kirka
Oak Ridge National Laboratory, Oak Ridge, Tennessee

Sheldon L. Semiatin
Air Force Research Laboratory, Wright-Patterson Air Force Base, Ohio

Timothy M. Smith and Christopher A. Kantzos
Glenn Research Center, Cleveland, Ohio

NASA STI Program . . . in Profile

Since its founding, NASA has been dedicated to the advancement of aeronautics and space science. The NASA Scientific and Technical Information (STI) Program plays a key part in helping NASA maintain this important role.

The NASA STI Program operates under the auspices of the Agency Chief Information Officer. It collects, organizes, provides for archiving, and disseminates NASA's STI. The NASA STI Program provides access to the NASA Technical Report Server—Registered (NTRS Reg) and NASA Technical Report Server—Public (NTRS) thus providing one of the largest collections of aeronautical and space science STI in the world. Results are published in both non-NASA channels and by NASA in the NASA STI Report Series, which includes the following report types:

- TECHNICAL PUBLICATION. Reports of completed research or a major significant phase of research that present the results of NASA programs and include extensive data or theoretical analysis. Includes compilations of significant scientific and technical data and information deemed to be of continuing reference value. NASA counter-part of peer-reviewed formal professional papers, but has less stringent limitations on manuscript length and extent of graphic presentations.

- TECHNICAL MEMORANDUM. Scientific and technical findings that are preliminary or of specialized interest, e.g., "quick-release" reports, working papers, and bibliographies that contain minimal annotation. Does not contain extensive analysis.

- CONTRACTOR REPORT. Scientific and technical findings by NASA-sponsored contractors and grantees.

- CONFERENCE PUBLICATION. Collected papers from scientific and technical conferences, symposia, seminars, or other meetings sponsored or co-sponsored by NASA.

- SPECIAL PUBLICATION. Scientific, technical, or historical information from NASA programs, projects, and missions, often concerned with subjects having substantial public interest.

- TECHNICAL TRANSLATION. English-language translations of foreign scientific and technical material pertinent to NASA's mission.

For more information about the NASA STI program, see the following:

- Access the NASA STI program home page at http://www.sti.nasa.gov

- E-mail your question to help@sti.nasa.gov

- Fax your question to the NASA STI Information Desk at 757-864-6500

- Telephone the NASA STI Information Desk at 757-864-9658

- Write to:
  NASA STI Program
  Mail Stop 148
  NASA Langley Research Center
  Hampton, VA 23681-2199

NASA/TM-20230002108

Competition of Failure Modes in an Additively Manufactured Disk Superalloy

Timothy P. Gabb and Chantal K. Sudbrack
Glenn Research Center, Cleveland, Ohio

Michael M. Kirka
Oak Ridge National Laboratory, Oak Ridge, Tennessee

Sheldon L. Semiatin
Air Force Research Laboratory, Wright-Patterson Air Force Base, Ohio

Timothy M. Smith and Christopher A. Kantzos
Glenn Research Center, Cleveland, Ohio

National Aeronautics and
Space Administration

Glenn Research Center
Cleveland, Ohio 44135

March 2023

Acknowledgments

Level of Review: This material has been technically reviewed by technical management.

Competition of Failure Modes in an Additively Manufactured Disk Superalloy

Timothy P. Gabb and Chantal K. Sudbrack[*]
National Aeronautics and Space Administration
Glenn Research Center
Cleveland, Ohio 44135

Michael M. Kirka
Oak Ridge National Laboratory
Oak Ridge, Tennessee 37830

Sheldon L. Semiatin
Air Force Research Laboratory
Wright-Patterson Air Force Base, Ohio 45433

Timothy M. Smith and Christopher A. Kantzos
National Aeronautics and Space Administration
Glenn Research Center
Cleveland, Ohio 44135

Summary

Additive manufacturing of powder metallurgy (PM) disk superalloys can produce unique microstructures that differ from those usually encountered in traditional processing as the result of consolidation, forging, and heat treatments. Unusual variations in grain size, major and minor phase precipitate sizes, and defects can occur. The failure modes associated with these unique microstructures are of high interest. The objective of this study was to compare the failure modes for a low solvus, high refractory (LSHR) PM disk superalloy produced by electron-beam-melting additive manufacturing. Specimens were subsequently given different solution heat treatments and a fixed aging heat treatment. Tensile, creep, and fatigue failure modes were screened in tests at elevated temperatures. Failure modes were considered with respect to these unique microstructures.

Introduction

Additive manufacturing generally refers to fabrication processes in which materials are built layer by layer rather than being machined from larger shapes, which is often called subtractive manufacturing. Over the years, many coating processes have been used to add successive layers of metal, including physical vapor deposition, plasma spray deposition, and cold spray. These processes are often used for symmetric shapes that allow open and uniform paths for deposition. More recently, advanced additive manufacturing approaches are being developed to build complex shapes layer by layer; these approaches use more complicated deposition processes.

Additive manufacturing processes for metallic alloy production have been comprehensively reviewed by Frazier (Ref. 1) and by Sames et al. (Ref. 2). In powder bed melting, a layer of powder is applied at a

---

[*]Currently with the U.S. Department of Energy National Energy Technology Laboratory.

controlled thickness onto a surface or bed, then carefully melted in a repetitive sequence. This localized melting is accomplished by rastering a laser beam or an electron beam across the layer of powder in carefully controlled patterns. Other approaches involve dynamically heating a surface with a similar beam to melt it, then adding more material as powder or wire, in a repetitive sequence. These varied processes are usually performed in inert gas or vacuum to prevent environmental contamination. Each of these processes involves compromises in surface roughness, near-surface porosity, cracking, residual stresses, and microstructures that must be addressed. These issues can be addressed for different alloys by subsequent sintering, hot isostatic pressing, heat treatment, and surface machining.

Applications of these advanced additive manufacturing processes to some nickel-based superalloys have been promising, especially using powder beds with laser beam or electron beam melting (Refs. 1 to 10). Surface finish and microstructural compromises are addressed well for superalloys that have relatively low levels of precipitate strengthening and that are weldable, such as Inconel® 625 (Special Metals Corporation) (Refs. 3 to 5) and superalloy 718 (Refs. 6 to 10). This includes optimization of additive manufacturing processes, subsequent hot isostatic pressurizations, heat treatments, and surface finishes (Ref. 10).

For the powder bed approaches applied to nickel-based superalloys, laser beam melting processes have generally produced better surface roughness and manageable levels of porosity but higher residual stresses (Ref. 3). The high residual stresses have been attributed to rapid convection plus radiation surface cooling in the inert gas environment interacting with slower heat conduction through cooler solidified material and the build plate below the surface, producing large temperature gradients between the deposited material and the solid layer onto which it is being deposited (Refs. 11 and 12). Electron beam melting processes can produce lower residual stresses and a reduced tendency for associated cracking than for laser beams, due in large part to slower cooling by only radiation in vacuum (Refs. 6 and 8) interacting with cooler solidified material below the surface as well as the build plate. Electron beam melting can produce comparable porosity, but it often results in higher surface roughness than laser beam melting. In both melting processes, unique microstructures have been observed (Refs. 4 and 13). Dendritic chemical segregation often encourages primary dendrites oriented in the building direction, transverse to the powder bed. Many of the solidified grains can be elongated in the building direction after fabrication, and oriented near the preferred [001] crystal growth direction of the nickel-rich γ phase. Minor phases such as carbides and borides can be elongated and grouped in lines parallel to the building direction (Ref. 14).

Nickel-based superalloys with higher levels of γ′ strengthening phase could potentially provide superior mechanical performance at elevated temperatures for additively manufactured components, in comparison to that of superalloys 625 and 718. Of these, superalloys used for turbine blade applications have the highest γ′ contents of 60 to 70 percent and corresponding highest creep resistances, especially when directionally solidified to produce elongated grains or even a single crystal near the [001] crystallographic orientation (Ref. 15). However, these superalloys have been more challenging to produce by additive manufacturing. Laser beam melting of powder beds using alloy MAR-M247 (Ref. 11), IN738LC (Ref. 13), and CMSX-4 (Ref. 16) have required extensive experimentation and modeling to deal with cracking problems; the same properties that lead to high creep strength resist relaxation of residual stresses from additive manufacturing. Electron beam melting with its associated slower cooling rates has shown better progress and has produced some promising results (Ref. 14). Directionally solidified grains have been preserved in combination with sufficiently fine γ′ precipitate size in Rene 142 (Ref. 17); directionally solidified grains and even single crystal specimens have been attained for CMSX-4 (Refs. 18 and 19). However, only a very limited supply of atomized powder is available for such blade superalloys.

Turbine disk superalloys currently developed for conventional powder metallurgy (PM) processing paths could offer interesting compromises for high-temperature applications of additively manufactured components. These superalloys could combine less severe processing challenges with high performance at elevated temperatures. Their lower levels of γ′ strengthening phase at 45 to 55 percent allow improved stress relaxation at high processing temperatures when compared to turbine blade superalloys. The PM disk superalloys have generally lower levels of refractory elements such as W, Ta, and Hf, for potentially lower levels of chemical segregation after additive manufacturing, when compared to the blade superalloys. These disk superalloys have carefully controlled low levels of minor elements C, B, and Zr to help strengthen grain boundaries. The disk superalloys have generally higher levels of ductility after conventional PM processing than is typical for blade superalloys, which could help maintain the integrity of additively manufactured components during processing. Various superalloy powder providers have ample experience atomizing and handling the powder for these disk superalloys, and can produce well-understood powder yields with minimized contaminants.

Initial work in producing one such disk superalloy using electron beam melting has shown much promise (Ref. 20). However, the previously cited references indicate that these additive manufacturing processes can produce varied and unique microstructures, with some attributes not usually encountered for these disk superalloys. These unique microstructures could influence various mechanical properties and associated failure modes. Because these superalloys were designed for high fatigue resistance in disk applications, the additive manufacturing processes described previously could be challenged to meet such fatigue design goals (Refs. 21 and 22).

Additive manufacturing processes are being suggested for producing various components at very close to near-net shape, with minimal subsequent machining. In some cases (Refs. 1 and 2), parts potentially could progress all the way from electron beam melted alloy powder to final product without removal of specimens from excess material to verify mechanical properties at various stages in the process. However, it is possible that a limited number of verification specimens could be produced along with or attached to a component to allow limited tests. These limited tests could screen mechanical properties as well as governing failure modes after all processing is completed. In such cases, it will be necessary to determine key mechanical properties with very few specimens and tests.

The objective of this study was to screen mechanical properties and failure modes for a low solvus, high refractory (LSHR) PM disk superalloy having widely varied microstructures produced by electron-beam-melting additive manufacturing. Limited mechanical tests were performed for initial screening of monotonic tensile and creep rupture failure modes. Fatigue tests were also performed at one temperature to allow initial evaluations of cyclic failure modes. The additively manufactured microstructures and prevalent failure modes for this alloy were then considered in comparison to those for microstructures of conventionally processed materials.

Materials and Procedures

The LSHR (Ref. 23) powder was atomized in argon by ATI Specialty Materials. The powder was selectively screened to have particle sizes between 45 μm and 106 μm. Electron beam melting was used to fabricate mechanical test blanks at the Oak Ridge National Laboratory's Manufacturing Demonstration Facility, using a customized Arcam S12 electron beam melting powder bed system. This system was employed with a stainless steel preheated build plate using 50-μm-thick build layers, in a controlled helium atmosphere. Four build sets were produced with consistent build parameters and configurations.

Two different solution heat treatment conditions, followed by a conventional aging heat treatment of 855 °C for 4 h plus 775 °C for 8 h, were selected for this evaluation. Solution heat treatment temperatures

were targeted at lower than the γ′ precipitate solvus temperature (subsolvus) and higher than the γ′ solvus temperature (supersolvus). The subsolvus solution condition (SUB2) was 1140 °C for 2 h. The supersolvus heat treatment condition (SUP2) selected was 1171 °C for 2 h. The average cooling rate of the blanks at completion of the solution heat treatments was controlled to be about 40 °C/min. The solution heat treatments were performed at Quintus Technologies under hot isostatic pressure, in groups of eight blanks that were randomly selected from the four different builds. The aging heat treatment was later performed in air at atmospheric pressure.

Microstructures were examined from sections prepared parallel and transverse to the build direction, *Z*. Additional details on microstructural evaluation techniques are provided in Reference 20. Elevations with respect to *Z* were examined near the build plate, at midbuild, and near the top. Optical and scanning electron microscopy was employed to examine grain and precipitate microstructures, and x-ray diffraction was used to assess grain texture. Samples were polished using SiC grit polishing paper followed by a 0.05 μm colloidal silica finish. To enhance optical imaging of grain boundaries, a waterless Kalling's etchant consisting of 100 mL hydrochloric acid, 100 mL methanol, and 5 g cupric chloride was applied with a swab. Line intercept methods were used for measuring average grain width.

To highlight the γ′ precipitates, an etchant that preferentially attacks the precipitates, consisting of 50 mL lactic acid, 30 mL nitric acid, and 2 mL hydrofluoric acid was applied with a swab. The latter etched surfaces were imaged using a Tescan MAIA$_3$ scanning electron microscope at 25 kV accelerating voltage while in analysis mode and utilizing the built-in Everhart–Thornley secondary electron detector. This imaging mode was found to provide a sufficient grayscale contrast between the etched γ′ precipitates and unetched γ matrix. The images were segmented using the adaptive threshold plug-in within the open-source ImageJ imaging program (Ref. 24). The threshold plug-in segments the image using the grayscale contrast between the darker etched γ′ precipitates and lighter γ matrix. The program determined a grayscale cutoff and minimum size of a precipitate. Any pixel determined to be dark enough to be considered a precipitate also had to have a minimum number of connecting dark pixels for it to be considered a precipitate and included in the segmentation step. Otherwise, the plug-in considered that pixel as noise and excluded it. The parameters for these settings were consistent across both heat treatments with respect to the imaged length scale. Because the γ′ microstructures were either bimodal or trimodal in nature, different magnifications were used to quantify the size and area fractions of each class (primary, secondary, or tertiary) of γ′ precipitate. An example of the original image of an etched surface resulting from the SUP2 heat treatment and the processed image is shown in Figure 1. From this processed image, only secondary γ′ precipitates were quantified. Higher magnification images were used to quantify tertiary γ′ precipitates.

Mechanical tests were chosen for evaluation to screen tensile, creep, and fatigue failure modes efficiently. A servohydraulic test system employing an axial extensometer and resistance heating furnace was used to perform conventional tensile fast (TF) fracture tests per ASTM E8 at room temperature and ASTM E21-17 (Ref. 25) at 704 °C and 760 °C. These tests were initiated at a constant strain rate of 0.5 percent/min, interrupted at 2 percent strain, and then run to failure under displacement control to produce an approximate strain rate of 5 percent/min. Tensile-stress relaxation-slow (TS) fracture tests were performed in the same system and again initiated at a constant strain rate of 0.5 percent/min. However, these tests were interrupted at 1 percent strain, and held at 1 percent strain while measuring stress as it relaxed for 100 h. The TS tests were subsequently continued to failure under displacement control with the slow approximated strain rate of 0.5 percent/min. Creep tests were performed at Metcut Research Inc. per ASTM E139-11 (Ref. 26) using lever arm creep machines employing an axial extensometer and resistance heating furnace. Fatigue tests were performed in a servohydraulic test system employing a resistance heating furnace. The load was cycled at a frequency of

0.33 Hz per ASTM E466-15 (Ref. 27) to produce an approximate maximum stress of 739 MPa and a minimum stress of –85 MPa (739 MPa/–85 MPa), or approximately 841 MPa/–427 MPa. The latter cyclic stresses were the values stabilized in prior tests of conventionally processed LSHR with continued strain cycling per ASTM E606-12 (Ref. 28) at 760 °C using a total strain range = 0.76 percent and strain ratio of minimum/maximum strain = 0. Optical microscopy and scanning electron microscopy were performed on fracture surfaces, as well as metallographic sections prepared parallel to the loading direction.

Results

Composition/Microstructure

Average composition in wt% as measured by inductively coupled plasma (ICP) spectroscopy is listed in Table I. This composition is very close to that of previously tested LSHR material that had been processed using conventional PM processing (Refs. 23 and 29). Microstructures were comprehensively studied and described in Reference 20, and are briefly summarized here. The typical grain structures varied with heat treat condition in terms of preferred orientation and size, as shown in Figure 2. The subsolvus heat treated (SUB2) material had grains elongated in the build direction Z, with preferred crystallographic orientations in the build direction near [001]. Some of these grains were as long as 819 µm in the build direction. However, these elongated grains were intermixed with scattered colonies of smaller, more equiaxed grains as short as 12 µm in the build direction, which were indicative of localized recrystallization. This resulted in highly variant linear intercept measurements parallel to the build direction. Grain size here as measured transverse to the build direction was more consistent, averaging 38 µm. The supersolvus heat treated (SUP2) material had more equiaxed grains, with no detected preference in crystallographic orientations. An average grain width of 86 µm was measured here and reported along with heat treat condition in Figure 2, signifying that the supersolvus heat treatment encouraged full recrystallization and progressive grain growth.

Typical γ′ sizes and contents also varied with heat treatment as detailed in Reference 20. Typical images from metallographically prepared cross sections of the gripped threaded sections from the TF test specimens are shown in Figure 3. The quantified γ′ precipitate area fractions and average sizes are listed in Table II and Table III. SUB2 material presented the expected trimodal γ′ size distribution. However, the coarse primary γ′ precipitates had an average diameter of 655 nm, which is distinctly finer than the primary γ′ around 1,000 nm usually encountered in conventional PM materials given subsolvus solution heat treatments (Ref. 23). SUP2 material presented the expected bimodal γ′ microstructure with the finer secondary precipitates averaging sizes near 275 nm and tertiary precipitate diameters near 30 nm. The most notable difference is a significantly lower area fraction of secondary γ′ precipitates in the SUB2 material in comparison to the SUP2 material. This observation remained consistent for different grains and between etched and unetched surfaces. This can be attributed in part to the presence of primary γ′ precipitates in the SUB2 material. The shorter cooling path of the SUB2 material also would be expected to have influences on the content and size of secondary γ′ precipitates.

Failure Responses

Tensile Failure Response

Typical surfaces of tensile fast (TF) fractures at room temperature for specimens loaded parallel and transverse to the building direction are shown in Figure 4 and Figure 5, respectively. SUP2 had ductile cup-cone failures, with transgranular microvoid coalescence at the center, and surface shear lips made up of discontinuous slip failures of large grains mixed with microvoid coalescence. SUB2 ductile failures had a similar makeup with smaller shear lips, and a nonmetallic (N) inclusion was also activated in

transverse loading. In these failures, SUP2 typically had higher tensile strengths than SUB2 specimens when loaded parallel or transverse to the building direction, with similar ductilities as indicated by reduction in area.

Longitudinal sections metallographically prepared on a plane parallel to the loading direction of these fractures are shown in Figure 6 and Figure 7. These sections confirmed the microvoid coalescence, notable slip deformation of grains, and predominantly transgranular failures. No surface cracks at grain boundaries were observed.

Typical surfaces of tensile fast (TF) fractures at 704 °C for specimens loaded parallel and transverse to the building direction are compared in Figure 8 and Figure 9, respectively. SUP2 failures were again dominated by transgranular slip of large grains near the surface, and grain slip failures mixed with microvoid coalescence near the center, here with a less consistent cup-cone profile. Conversely, SUB2 had a more pronounced cup-cone profile with surface shear lips than in tests at room temperature. Along with these grain slip and microvoid coalescence trends of SUP2 failures, SUB2 fractures included minor intergranular (IG) grain failures near or at the exposed surface. For these failures, SUP2 again had higher tensile strengths than SUB2 specimens when loaded parallel or transverse to the building direction. Ductilities were significantly reduced for SUP2 and SUB2 specimens loaded in the transverse direction at 704 °C, in comparison to the cases mentioned previously.

Typical surfaces of tensile slow (TS) fractures at 704 °C for specimens loaded parallel and transverse to the building direction are depicted in Figure 10 and Figure 11, respectively. SUP2 failures were still dominated by slip failures of large grains, along with a few minor surface cracks starting at grain boundaries. SUB2 failures initiated from intergranular cracks at the exposed surface. For these failures, SUP2 again had higher tensile strengths than SUB2 specimens when loaded parallel or transverse to the building direction. Ductilities were significantly reduced for SUP2 and SUB2 specimens loaded parallel to the building direction, in comparison to that measured in tensile fast fracture tests.

Typical surfaces of tensile slow (TS) fractures at a higher temperature of 760 °C for specimens loaded parallel and transverse to the building direction are presented in Figure 12 and Figure 13, respectively. All material failures were initiated in these conditions from intergranular cracks at the exposed surface. The extent of these surface-initiated intergranular cracks increased at this higher test temperature. Neither the elongated grains of SUB2 nor the larger grains of SUP2 could block this environment-assisted surface cracking mode at 760 °C. This failure mode was previously observed to be dominant for conventionally processed materials in tensile slow tests at 704 °C to 815 °C (Ref. 30). In these tensile slow failures at 760 °C, SUP2 continued to have higher strengths than SUB2 specimens in loading parallel or transverse to the building direction. However, these SUP2 specimens had lower ductilities than for SUB2.

Cross sections prepared on a plane parallel to the loading direction from fracture surfaces for tensile slow fractures at 760 °C are depicted in Figure 14 and Figure 15. Although most material failures were confirmed to initiate from intergranular cracks at the exposed surface, internal cracks were also observed at scattered colonies of fine grains present in SUB2 specimens.

Creep Failure Response

Typical fracture surfaces from creep rupture tests performed at 760 °C and 620 MPa for specimens loaded parallel and transverse to the building direction are shown in Figure 16 and Figure 17. Large surface cracks initiated the failures for all SUP2 and SUB2 specimens, and they initially grew along grain boundaries. These cracks grew further in the creep rupture specimens in comparison to the tensile slow fractures at 760 °C. However, the failure mode looked very similar to those in the slow strain rate tensile slow tests, with similar levels of initial intergranular cracking. In this respect, the tensile slow tests could be a useful screening tool for a material's resistance to this cracking mode. This failure mode also was

previously observed to be dominant for conventionally processed materials in creep tests at 704 °C to 815 °C (Ref. 23). No clear trend in rupture life could be discerned between heat treatments and loading directions. However, the SUP2 specimen loaded transverse to the building direction had only a 5.4 percent reduction in area, the lowest ductility value observed in all these monotonic tensile and creep rupture tests.

Metallographic sections were prepared on a plane parallel to the loading direction, across the failure initiation points of creep rupture specimens loaded parallel and transverse to the building direction. As shown in Figure 18 and Figure 19, surface cracks grew along grain boundaries to cause failures. Secondary cracks also sometimes initiated internally at colonies of fine grains for creep tested SUB2 specimens. Such internal cracks had also been observed in slow tensile fractures of SUB2 specimens.

Fatigue Failure Response

Typical fracture surfaces from fatigue tests performed at 760 °C are shown in Figure 20 to Figure 23. For specimens tested at the larger applied approximate maximum/minimum stresses of 841 MPa/–427 MPa, fatigue failures of SUP2 and SUB2 specimens were usually initiated from slip-induced failure of relatively large grains in the microstructure, as shown in Figure 20 and Figure 21. Subsequent growth of cracks was predominantly transgranular.

For specimens tested at the lower applied approximate maximum/minimum stresses of 739 MPa/ –85 MPa, SUP2 and SUB2 failures were more often initiated from nonmetallic inclusions, as shown in Figure 22 and Figure 23. These inclusions were predominantly composed of aluminum and oxygen, consistent with alumina crucibles or lining materials in vacuum induction melting systems that are used to melt superalloys prior to gas atomization. Their size, near 100 μm, was larger than that typically observed in conventionally processed PM superalloys, including LSHR (Ref. 23). This size was within the size distribution of superalloy powder used here for additive manufacturing. The growth of the cracks at this lower applied fatigue stress was also predominantly transgranular.

Discussion

Microstructures

An interesting mixture of elongated grains with colonies of fine, more equiaxed grains was observed in SUB2 material. This microstructure had not been encountered during conventional processing of LSHR, and was therefore attractive to test. Conversely, the supersolvus heat treated material SUP2 had more uniform but unusually coarse grain size. Significantly coarser grain sizes were obtained for supersolvus heat treatments of the present additively manufactured LSHR, in comparison to that obtained using conventional PM processing (Refs. 20, 23, and 29). This markedly coarse grain size attained in the present material therefore also represented a unique microstructural attribute for this PM superalloy that warranted testing. The very coarse grain microstructure in SUP2 was expected to impair strength in comparison to the finer grain sizes of conventionally processed material, but the mixed grain structure in SUB2 was more uncertain (Ref. 31).

The constraints limiting grain growth during supersolvus heat treatment for the present additively manufactured material clearly differs from that usually observed for conventional PM processing. The pinning points that usually constrain grain growth (Ref. 29) appear to be altered in the present materials. It is apparent that the very fine oxides, carbides, and nitrides along prior powder particle boundaries that survive after conventional consolidation, extrusion, and forging did not remain fine after electron beam melting. Stringers of MC carbides aligned in the build direction were observed in the as-built materials, along with significant dendritic segregation in composition across and along the build direction (Ref. 20). Assuming similar volume fractions (f) of carbides/oxides, the coarser γ grain sizes in these samples after

supersolvus heat treatment could be partially explained by Zener-pinning effects, for which the pinned grain size is proportional to r/f in which r denotes the (average) radius of the pinning particles. Furthermore, the distributed coarse primary γ′ particles 1 μm to 5 μm in diameter that are usually observed before heat treatment in extruded and forged materials are refined in size here. The unusual morphologies for these important grain boundary pinning points can help explain the grain structures observed here. Additional work is necessary to fully quantify and understand these aspects, and how they can potentially be used for controlling grain size in future processing.

These materials also had divergent γ′ sizes and contents, which could influence strength. SUB2 material had a consistent trimodal γ′ size distribution. The γ′ size distribution for this subsolvus solution heat treated plus aged material appears to be unique, and is not typically observed for conventional PM processing. The coarse γ′ observed here near 650 nm in size is distinctly finer than primary γ′ around 1,000 nm usually encountered in conventional PM materials given subsolvus solution heat treatments. For conventionally processed superalloys, the size of primary γ′ is largely set during extrusion/recrystallization at subsolvus temperatures. The evolution of what is called primary γ′ in the present samples after subsolvus solution heat treatment appears to be more complicated. It would evolve during (1) multiple thermal cycles both higher and lower than the solvus temperature during additive manufacturing, (2) time at temperatures less than the solvus temperature (especially for layers that are lower in the build) during additive manufacturing, (3) cooldown once all layers have been deposited during additive manufacturing, (4) reheating to and dwell time at the solution temperature during which γ′ dissolution occurs, which can result in a finer average (primary) γ′ particle size (Ref. 32), and (5) some very limited γ′ particle growth during final cooling before the on-cooling secondary and/or on-cooling tertiary γ′ are formed. The primary γ′ would finally grow a very small amount during cooling following soak at the subsolvus solution temperature. Models now exist that could potentially account for these effects on microstructure and strength (Ref. 32). Conversely, the supersolvus heat treated material SUP2 had uniform secondary γ′ near 250 nm and tertiary γ′ near 30 nm, both comparable to those observed in conventionally processed materials.

Failure Responses and Predominant Failure Modes

The mechanical responses of all these presented specimens are summarized in Table IV. The modestly lower ultimate strengths observed for these additively manufactured materials in comparison to conventional PM-processed materials (Ref. 23) can be attributed to several factors. Although the uniform fine secondary and tertiary γ′ sizes of the supersolvus heat treated SUP2 material were comparable to those for conventionally processed material, the unique coarse grain sizes in SUP2 could be expected to impair strength through reduced grain size strengthening (Ref. 31). Yet, this inverse dependence between strength and average grain size was complicated by the mixed unidirectional large grains with colonies of finer equiaxed grains in the SUB2 material. SUP2 materials consistently had the higher strength, suggesting a more favorable compromise in grain size distribution for strength than that apparent for SUB2. The different size distributions of γ′ precipitates between SUP2 and SUB2 also should be factored into this comparison.

Ultimate strengths measured in tensile fast and tensile slow tests were consistently lower for SUB2 in comparison to supersolvus heat treated SUP2. The lower strength of SUB2 compared to SUP2 samples can be related to the texture (001 for SUB2 and random for SUP2, Ref. 20). The Taylor factors for a [001] texture and a random texture (pulled in axisymmetric tension) are approximately 2.44 and 3.06 (Ref. 33), respectively. This texture may also contribute to the lower surface cracking resistance of SUB2, which will be further considered in subsequent paragraphs.

In the tensile fast tests, along with traditional transgranular microvold coalescence, the present materials did display prominent slip plane failures of relatively large grains in the failure regions of the SUP2 and SUB2 materials. Although grain slip failures are sometimes reported in analogous conventionally processed materials (Ref. 23), the large grains encountered in the present materials gave this failure mode more prominence and potential influence. This could help explain the lower ductilities sometimes observed here in comparison to conventionally processed materials.

The reductions in strength and ductility with the slow strain rate of the tensile slow tests in comparison to the tensile fast tests have also been observed in conventionally processed LSHR (Ref. 23). The failure modes observed in these tensile fast versus tensile slow tests generally followed those of the conventionally processed material. Tensile fast failures were dominated by ductile shear lips near the surface, with ductile failure by microvoid coalescence in the center. Yet, the prominence of slip failures of large grains was not noted in prior work. Intergranular cracks initiated at the surface dominated failures in the tensile slow tests. Ten out of ten specimens failed from these cracks in tensile slow tests at 704 °C, 760 °C, and 815 °C. This was accompanied by a reduction in measured ductility. These aspects have also previously been observed for several other conventionally processed disk superalloys and related to environment-assisted surface cracking (Refs. 23 and 30).

Comparisons of the creep failures for the SUB2 and SUP2 materials extended the previously mentioned trends in failure mode. The slower strain rates observed during creep tests encouraged even larger intergranular cracks that had been initiated at the surface, which were most apparent for specimens loaded transverse to the building direction. All five creep specimens tested at this condition failed from these cracks. Overall, 10 out of 10 specimens failed from these intergranular surface cracks in creep tests at 704 °C, 760 °C, and 815 °C. It is notable that, although microstructures consisting of γ grains elongated parallel to the loading direction are often observed to exhibit improved creep resistance (Ref. 15), the elongated γ grain microstructures observed in SUB2 material did not appear to be as effective here. This may signify the overwhelming influence of the environment in encouraging this dominant failure mode. Creep tests in vacuum are being considered to further evaluate this influence. However, the SUB2 material apparently also had shortcomings associated in part with a lack of uniformity. The failures of grain boundaries observed at interior colonies of fine grains for these creep specimens may have reduced the effectiveness of the elongated grains. In comparison, the more uniform, unusually coarse γ grain sizes attained in supersolvus heat treated materials appeared to play a more dominant role in creep resistance. Their response exceeded that of conventionally processed materials having finer γ grain sizes than attained here (Ref. 23).

Additional testing would be required for rigorously comparing the rupture resistances of SUB2 and SUP2 materials. However, the existing test results suggest that SUB2 and SUP2 specimens loaded transverse to the building direction could have lower response than those loaded parallel to the building direction. The lower rupture lives and ductilities observed here were accompanied with failures of long grain boundaries transverse to the loading direction. This was most noticeable for the SUB2 material as shown in Figure 17. The shearing of γ' precipitates also generally plays an important role in limiting creep rupture of superalloys at these test conditions (Ref. 34). Additional work would be necessary to compare these deformation modes for the unique microstructures tested here.

In summary, creep rupture lives and failures were generally comparable to that of conventionally processed materials, with similar intergranular cracks that were initiated at the surface and grew into the cross section. This has been related to an alloy and microstructures' resistance to environment-assisted surface cracking (Refs. 23 and 30).

Initial screening tests indicate the fatigue resistance of the present SUB2 and SUP2 materials was lower than that observed in conventionally processed materials. As noted previously, the tensile strength was lower than that of conventional materials, and this would be expected to impair fatigue life (Ref. 34).

The fatigue failure modes operative in SUB2 and SUP2 materials can also help explain the lower lives observed here. At high applied fatigue stresses, three out of four SUP2 specimens failed from slip failures of large grains. This grain "facet" failure mode has previously been observed in many conventionally processed disk superalloys, including LSHR (Ref. 23). However, the larger size of the grains in the present materials can justify the lower corresponding fatigue lives. It is expected that these slip failures occur in a single cycle, without incremental cyclic crack growth. For a given applied fatigue stress, these larger grains would thereby produce larger initial crack sizes and corresponding stress intensities for subsequent cyclic crack propagation. One other SUP2 specimen failed from an aluminum-rich oxide inclusion. So, it was apparent that slip failures more often limited the fatigue life of SUP2 material at these high applied stress conditions.

However, at the same high applied fatigue stresses, three out of four SUB2 specimens failed from aluminum-rich oxide inclusions; the other SUB2 specimen failed from the slip failure of a near-surface large grain. This indicated that cracks initiating at these nonmetallic inclusions could more often limit the fatigue life of SUB2 material at these same high stress conditions.

At lower applied fatigue stresses, four out of five SUP2 specimens failed from cracks initiated at nonmetallic inclusions. The other SUP2 specimen failed from slip failures of several adjacent large grains. Three out of three SUB2 specimens also failed from cracks initiating at the nonmetallic inclusions. This indicated that cracks initiating at these inclusions were more dominant in limiting the fatigue lives of both SUP2 and SUB2 material at these lower applied stress conditions.

These aluminum-rich oxide inclusions dominated the competition of fatigue failure modes, so they merited further scrutiny. The presented inclusions had some unique characteristics in comparison to those limiting fatigue life in conventionally processed PM superalloys such as LSHR (Ref. 23) and ME3 (Ref. 35). The present inclusions limiting fatigue life were larger in cross section and more undulating in shape when compared to those reported in many references. These observed characteristics could be related to the unique processing used in the present study. The input powder size distribution used here allowed larger superalloy and contaminant powder particles than in some of the referenced work. Furthermore, during additive manufacturing, the electron beam melting of each newly applied layer of superalloy powder would have melted any entrapped nonmetallic inclusions, to then resolidify upon cooling. These factors could account for the unusual size and shape of the observed inclusions that initiated fatigue failures. Tracking of such fatigue life-limiting nonmetallic inclusion contaminants from input powder to resultant inclusions in fully processed specimens deserves further study to establish input-output relationships. It appears that the more complex additive manufacturing process could significantly perturb these relationships, with respect to those generated using conventionally processed materials (Ref. 36).

Overall, although such additive manufacturing processes can produce microstructures having more coarse or elongated grains than those produced using conventional processing, their effects on mechanical properties will need careful consideration with respect to intended applications. Applications with static loading at relatively high temperatures could benefit from coarse grains giving improved creep resistance. However, the corresponding impacts on strength and fatigue resistance will need careful consideration with respect to intended applications. It may be that aerospace applications requiring fewer fatigue loading cycles but longer, creep-limited static loads could benefit more using the present materials. Meanwhile, fatigue-intensive applications may require further refinements in microstructures of this additively manufactured material.

Conclusions

Powder metallurgy disk superalloy low solvus, high refractory (LSHR) was consistently prepared using electron beam melting of a powder bed at fixed processing conditions. Heat treatments were used to vary its microstructure to give unique attributes not usually observed in this superalloy. Tensile, slow tensile, creep, and fatigue tests were performed for two selected microstructures. Tensile fast failures were associated with slip failures of large grains. Tensile slow and creep failures were initiated from environment-assisted cracking of surface grain boundaries as usually observed in conventionally processed materials. Fatigue failures at high applied stresses were often initiated from grain slip failures; however, at low cyclic stresses, fatigue failures were more often initiated at nonmetallic inclusions.

Several conclusions can be drawn from this work:

1. Additive manufacturing combined with varied subsequent heat treatments can produce a wide range of microstructures in γ' precipitate-strengthened disk superalloys, including unusually large or elongated grains.
2. Large or elongated grains may hinder but not prevent environment-driven intergranular surface cracks in tensile and creep tests, and they also can initiate tensile fast failures and fatigue failures in this material.
3. As with conventionally processed superalloys, inhomogeneities in additively manufactured microstructures such as colonies of fine grains can also be crack initiation sites that need to be monitored.
4. Nonmetallic inclusion contaminants can still limit fatigue resistance of these superalloys after additive manufacturing, even with these widely varied microstructures.
5. For applications encountering static loading near the tested temperatures, careful consideration would be necessary for these balances in superalloy microstructure and properties required for successful utilization.
6. For applications encountering fatigue loading, controls of nonmetallic inclusions during powder atomization, handling, and additive manufacturing would also need to be carefully screened.

References

1. Frazier, William E.: Metal Additive Manufacturing: A Review. J. Mater. Eng. Perform., vol. 23, 2014, pp. 1917–1928.
2. Sames, W.J.; List, F.A.; Pannala, S.; Dehoff, R.R.; and Babu, S.S.: The Metallurgy and Processing Science of Metal Additive Manufacturing. Int. Mater. Rev., vol. 61, no. 5, 2016, pp. 315–360.
3. Brown, Christopher U.; Jacob, Gregor; Stoudt, Mark; Moylan, Shawn; Slotwinski, John; and Donmez, Alkan: Interlaboratory Study for Nickel Alloy 625 Made by Laser Powder Bed Fusion to Quantify Mechanical Property Variability. J. Mater. Eng. Perform., vol. 25, 2016, pp. 3390–3397.
4. Murr, Lawrence E.; Gaytan, Sara M.; Ramirez, Diana A.; Martinez, Edwin; Hernandez, Jennifer; Amato, Krista N.; Shindo, Patrick W.; Medina, Francisco R.; and Wicker, Ryan B.: Metal Fabrication by Additive Manufacturing Using Laser and Electron Beam Melting Technologies. J. Mater. Sci. Technol., vol. 28, no. 1, 2012, pp. 1–14.
5. Li, C.; Guo, Y.B.; and Zhao, J.B.: Interfacial Phenomena and Characteristics Between the Deposited Material and Substrate in Selective Laser Melting Inconel 625. J. Mater. Process. Technol., vol. 243, 2017, pp. 269–281.
6. Sames, William J.; Unocic, Kinga A.; Dehoff, Ryan R.; Lolla, Tapasvi; and Babu, Sudarsanam S.: Thermal Effects on Microstructural Heterogeneity of Inconel 718 Materials Fabricated by Electron Beam Melting, J. Mater. Res., vol. 29, 2014, pp. 1920–1930.

7. Amato K.N.; Gaytan, S.M.; Murr, L.E.; Martinez, E.; Shindo, P.W.; Hernandez, J.; Collins, S.; and Medina, F.: Microstructures and Mechanical Behavior of Inconel 718 Fabricated by Selective Laser Melting. Acta Mater., vol. 60, no. 5, 2012, pp. 2229–2239.

8. Sochalski-Kolbus, L.M.; Payzant, E.A.; Cornwell, P.A.; Watkins, T.R.; Babu, S.S.; Dehoff, R.R.; Lorenz, M.; Ovchinnikova, O.; and Duty, C.: Comparison of Residual Stresses in Inconel 718 Simple Parts Made by Electron Beam Melting and Direct Laser Metal Sintering, Met. Trans. A, vol. 46, 2015, pp. 1419–1432.

9. Kirka, M.M.; Greeley, D.A.; Hawkins, C.; and Dehoff, R.R.: Effect of Anisotropy and Texture on the Low Cycle Fatigue Behavior of Inconel 718 Processed via Electron Beam Melting. Int. J. Fatigue, vol. 105, 2017, pp. 235–243.

10. Sudbrack, Chantal K.; Lerch, Bradley A.; Smith, Timothy Michael; Locci, Ivan; Ellis, David L.; Thompson, Aaron C.; and Richards, Benjamin: Impact of Powder Variability on the Microstructure and Mechanical Behavior of Selective Laser Melted Alloy 718. Proceedings of the 9th International Symposium on Superalloy 718 & Derivatives: Energy, Aerospace, and Industrial Applications, TMS, 2018, pp. 89–113.

11. Carter, Luke N.; Martin, Christopher; Withers, Philip J.; and Attallah, Moataz M.: The Influence of the Laser Scan Strategy on Grain Structure and Cracking Behavior in SLM Powder-Bed Fabricated Nickel Superalloy, J. Alloys Compds., vol. 615, 2014, pp. 338–347.

12. Carter, Luke N.; Attallah, Moataz M.; and Reed, Roger C.: Laser Bed Fabrication of Nickel-Base Superalloys: Influence of Parameters; Characterization, Quantification and Mitigation of Cracking. Superalloys 2012, TMS, Warrendale, PA, 2012, pp. 577–586.

13. Geiger, Fabian; Kunze, Karsten; and Etter, Thomas: Tailoring the Texture of IN738LC Processed by Selective Laser Melting (SLM) by Specific Scanning Strategies. Mater. Sci. Eng. A, vol. 661, 2016, pp. 240–246.

14. Korner, C.: Additive Manufacturing of Metallic Components by Selective Electron Beam Melting— A Review. Int. Mater. Rev., vol. 61, no. 5, 2016, pp. 361–377.

15. Gell, Maurice; Duhl, D.N.; and Giamei, A.F.: The Development of Single Crystal Superalloy Turbine Blades. Superalloys 1980, TMS, Warrendale, PA, 1980, pp. 205–214.

16. Basak, Amrita; Acharya, Ranadip; and Das, Suman: Additive Manufacturing of Single-Crystal Superalloy CMSX-4 Through Scanning Laser Epitaxy: Computational Modeling, Experimental Process Development, and Process Parameter Optimization. Metall. Mater. Trans. A, vol. 47, 2016, pp. 3845–3859.

17. Murr, L.E.; Martinez, E.; Pan, X.M.; Gaytan, S.M.; Castro, J.A.; Terrazas, C.A.; Medina, F.; Wicker, R.B.; and Abbott, D.H.: Microstructures of Rene 142 Nickel-Based Superalloy Fabricated by Electron Beam Melting. Acta Mater., vol. 61, no. 11, 2013, pp. 4289–4296.

18. Ramsperger, Markus; Singer, Robert F.; and Korner, Carolin: Microstructure of the Nickel-Base Superalloy CMSX-4 Fabricated by Selective Electron Beam Melting. Metall. Mater. Trans. A, vol. 47, 2016, pp. 1469–1480.

19. Ramsperger, Markus; and Korner, Carolin: Selective Electron Beam Melting of the Single Crystalline Nickel-Base Superalloy CMSX-4®: From Columnar Grains to a Single Crystal. Superalloys 2016, TMS, Warrendale, PA, 2016, pp. 341–349.

20. Sudbrack, Chantal K.; Kirka, Michael M.; Semiatin, S. Lee; and Gabb, Timothy P.: Location-Specific Microstructure and the Effect of Heat Treatment on Electron-Beam Melted Ni-Based Superalloy LSHR. TMS 2018 147th Annual Meeting and Exhibition, TMS, Warrendale, PA, 2018.

21. Yadollah, Aref; and Shamsaei, Nima: Additive Manufacturing of Fatigue Resistant Materials: Challenges and Opportunities. Int. J. Fatigue, vol. 98, 2017, pp. 14–31.

22. Gorelik, Michael: Additive Manufacturing in the Context of Structural Integrity. Int. J. Fatigue, vol. 94, part 2, 2017, pp. 168–177.

23. Gabb, Timothy P.; MacKay, Rebecca A.; Draper, Susan L.; Sudbrack, Chantal K.; and Nathal, Michael V.: The Mechanical Properties of Candidate Superalloys for a Hybrid Turbine Disk. NASA/TM—2013-217901, 2013. https://ntrs.nasa.gov

24. Abramoff, M.D.; Magalhaes, P.J.; and Ram, S.J.: Image Processing With ImageJ. Biophotonics Int., vol. 11, no. 7, 2004, pp. 36–42.

25. ASTM E21–17: Standard Test Methods for Elevated Temperature Tension Tests of Metallic Materials. ASTM International, West Conshohocken, PA, 2017.

26. ASTM E139–11(2018): Standard Test Methods for Conducting Creep, Creep-Rupture, and Stress-Rupture Tests of Metallic Materials. ASTM International, West Conshohocken, PA, 2018.

27. ASTM E466–15: Standard Practice for Conducting Force Controlled Constant Amplitude Axial Fatigue Tests of Metallic Materials. ASTM International, West Conshohocken, PA, 2015.

28. ASTM E606/E606M–12: Standard Test Method for Strain-Controlled Fatigue Testing. ASTM International, West Conshohocken, PA, 2012.

29. Semiatin, S.L.; McClary, K.E.; Rollett, A.D.; Roberts, C.G.; Payton, E.J.; Zhang, F.; and Gabb, T.P.: Microstructure Evolution During Supersolvus Heat Treatment of a Powder Metallurgy Nickel-Base Superalloy. Metall. Mater. Trans. A, vol. 43, 2012, pp. 1649–1661.

30. Gabb, Tim P.; Telesman, Jack; Banik, Anthony; and McDevitt, Erin: Use of Slow Strain Rate Tensile Testing to Assess the Ability of Several Superalloys to Resist Environmentally-Assisted Intergranular Cracking. Proceedings of the 8th International Symposium on Superalloy 718 and Derivatives, Pittsburgh, PA, 2014.

31. Parthasarathya, Triplicane A.; and John, Reji: A Microstructure-Sensitive Location-Specific Design Tool for Predicting the Yield and Creep Behavior of LSHR Ni-Base Superalloy. Mater. Sci. Eng. A, vol. 712, 2018, pp. 502–512.

32. Semiatin, S.L.; Levkulich, N.C.; Saurber, A.E.; Mahaffey, D.W.; Payton, E.J.; and Senkov, O.N.: The Kinetics of Precipitate Dissolution in a Nickel-Base Superalloy. Metall. Mater. Trans. A, vol. 48, 2017, pp. 5567–5578.

33. Smith, T.M.; Gabb, T.P.; Wertz, K.N.; Stuckner, J.; Evans, L.J.; Egan, A.J.; and Mills, M.J.: Enhancing the Creep Strength of Next Generation Disk Superalloys via Local Phase Transformation Strengthening. Superalloys 2020, TMS, Warrendale, PA, 2020, pp. 726–736.

34. Manson, S.S.; and Halford, Gary: A Method of Estimating High Temperature Low Cycle Fatigue Behavior of Materials. NASA TM X–52270, 1967. https://ntrs.nasa.gov

35. Gabb, T.P.; Telesman, J.; Kantzos, P.T.; and Garg, A.: Effects of Temperature on Failure Modes for a Nickel-Base Disk Superalloy. J. Fail. Anal. Prev., vol. 7, 2007, pp. 56–65.

36. Huron, Eric S., and Roth, Paul G.: The Influence of Inclusions on Low Cycle Fatigue Life in a P/M Nickel-Base Disk Superalloy. Superalloys 1996, TMS, Warrendale, PA, 1996, pp. 359–368.

TABLE I.—AVERAGE COMPOSITIONS IN WEIGHT PERCENT OF PRESENT ELECTRON
BEAM MELTED AND CONVENTIONALLY PROCESSED LSHR MATERIALS (REF. 23)

Weight %	Al	B	C	Co	Cr	Fe	Mo	Ni	Nb	Ta	Ti	Si	V	W	Zr	O
Present	3.51	0.025	0.038	20.42	12.14	0.015	2.75	Bal.	1.52	1.49	3.52	0.02	0	4.47	0.042	0.008
Conventional	3.54	0.027	0.045	20.4	12.3	0.1	2.71	Bal.	1.49	1.52	3.45	0.012	0.006	4.28	0.049	0.02

TABLE II.—THE AVERAGE γ' AREA PERCENTAGE FOR SUB2 AND SUP2 MATERIALS

Heat treatment	Primary	Secondary	Tertiary	Total	Total, standard deviation
SUB2	21.8	18.1	1.5	41.4	1.3
SUP2	NA	39.4	3.2	42.6	0.3

TABLE III.—THE AVERAGE SIZES IN DIAMETER (nm) OF PRIMARY, SECONDARY, AND
TERTIARY γ' PRECIPITATES FOR SUB2 AND SUP2 MATERIALS, COMPARED TO
CONVENTIONALLY PROCESSED SUPERSOLVUS HEAT TREATED MATERIALS
WITH AVERAGE GRAIN SIZES OF 15 μm AND 50 μm (REF. 23)

Heat treatment	Primary size	Secondary size	Tertiary size
SUB2	655.3	185.2	40.6
SUP2	NA	274.8	29.2
Conventional 15 μm	-------	248	30.2
Conventional 50 μm	-------	268	34.6

TABLE IV.—MECHANICAL RESPONSES OF PRESENTED SPECIMENS

Test type	Material	Building-loading orientation	Temperature, °C	Ultimate tensile strength or maximum stress, MPa	Life, h	Life, cycles	Reduction in area, %	Fracture figures
Tensile Fast (TF)	SUP2	Parallel	21	1,470	-------	--------	17.8	4, 6
TF	SUB2	Parallel	21	1,396	-------	--------	21.9	4, 6
TF	SUP2	Transverse	21	1,462	-------	--------	17.0	5, 7
TF	SUB2	Transverse	21	1,420	-------	--------	20.0	5, 7
TF	SUP2	Parallel	704	1,247	-------	--------	16.4	8
TF	SUB2	Parallel	704	1,234	-------	--------	28.6	8
TF	SUP2	Transverse	704	1,281	-------	--------	10.8	9
TF	SUB2	Transverse	704	1,205	-------	--------	9.2	9
Tensile Slow (TS)	SUP2	Parallel	704	1,207	-------	--------	6.3	10
TS	SUB2	Parallel	704	1,116	-------	--------	9.8	10
TS	SUP2	Transverse	704	1,200	-------	--------	14.7	11
TS	SUB2	Transverse	704	1,108	-------	--------	9.6	11
TS	SUP2	Parallel	760	1,017	-------	--------	9.1	12, 14
TS	SUB2	Parallel	760	979	-------	--------	13.4	12, 14
TS	SUP2	Transverse	760	1,020	-------	--------	10.4	13, 15
TS	SUB2	Transverse	760	965	-------	--------	12.2	13, 15
Creep Rupture	SUP2	Parallel	760	620	188.8	--------	13.5	16, 18
Creep Rupture	SUB2	Parallel	760	620	260.8	--------	27.9	16, 18
Creep Rupture	SUP2	Transverse	760	620	175	--------	5.4	17, 19
Creep Rupture	SUB2	Transverse	760	620	97.3	--------	16.2	17, 19
Fatigue	SUP2	Parallel	760	739	38.4	46,031	----	20
Fatigue	SUB2	Parallel	760	739	32.7	39,236	----	20
Fatigue	SUP2	Transverse	760	739	78.6	94,321	----	21
Fatigue	SUB2	Transverse	760	739	53.5	64,233	----	21
Fatigue	SUP2	Parallel	760	841	1.9	2,306	----	22
Fatigue	SUB2	Parallel	760	841	3.4	4,081	----	22
Fatigue	SUP2	Transverse	760	849	3.0	3,652	----	23
Fatigue	SUB2	Transverse	760	841	10.6	12,692	----	23
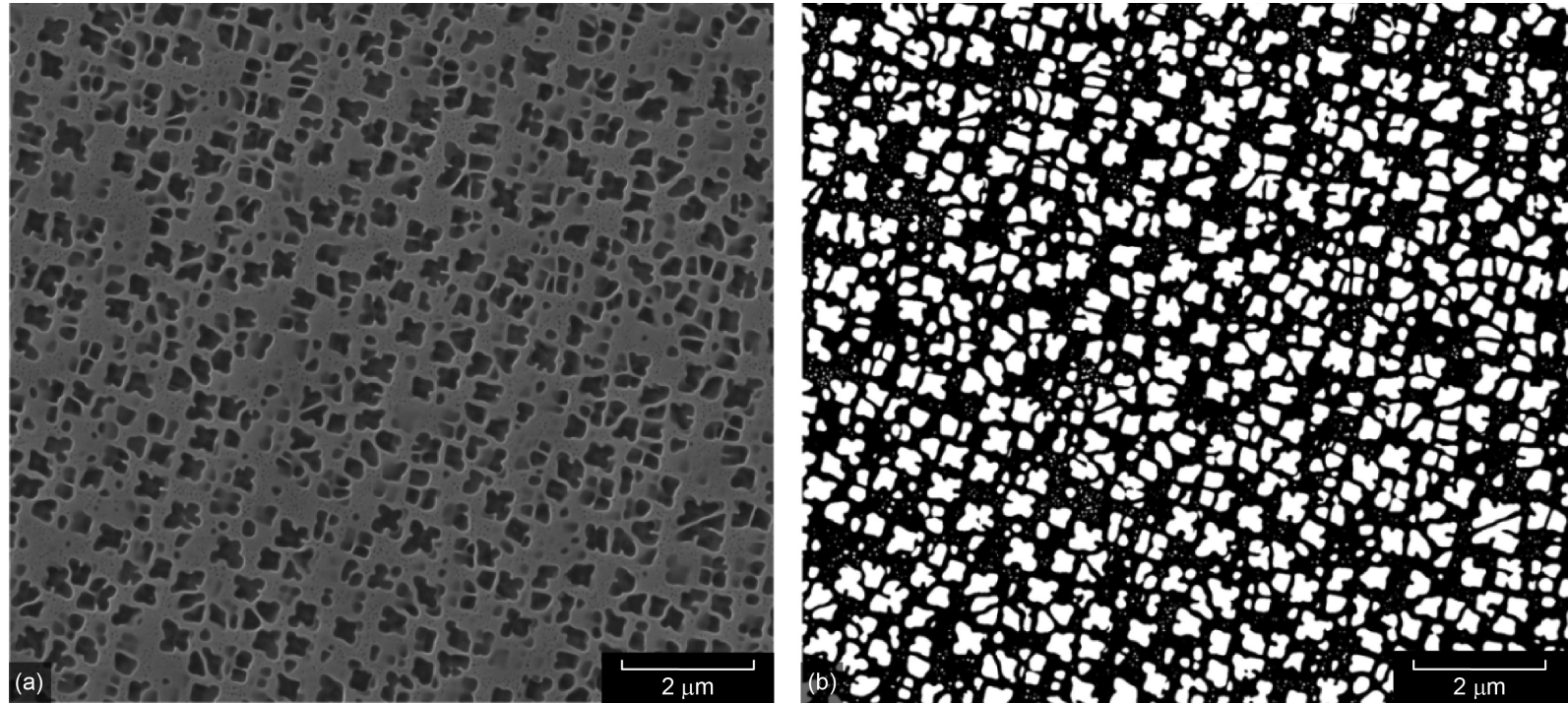
Figure 1.—(a) Etched γ/γ' microstructure in SUP2. (b) Segmented image used to derive secondary γ' precipitate size and area fractions. From this image only the secondary γ' precipitates were quantified. Higher magnification images were used to quantify the tertiary γ' precipitates.
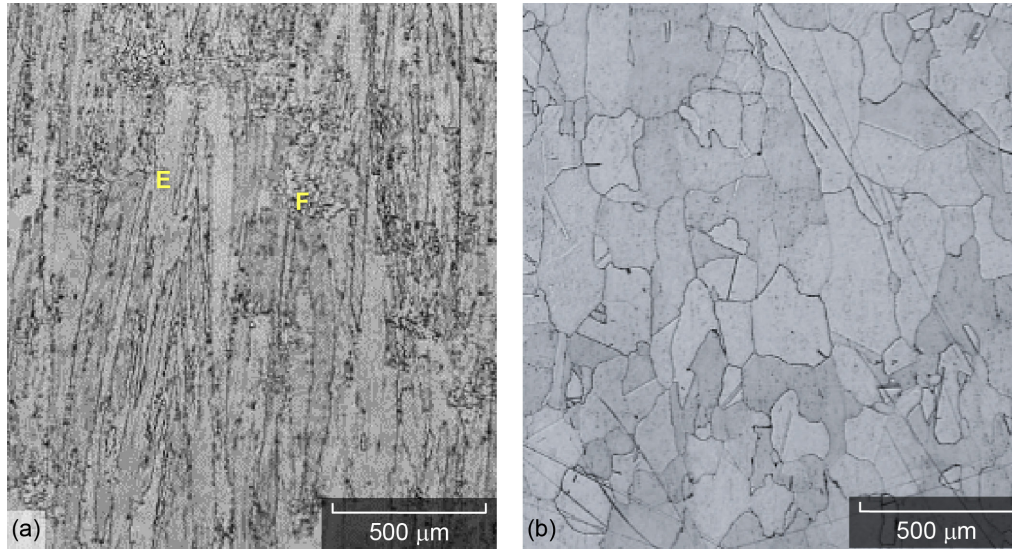
Figure 2.—Grain structures for test materials. Building direction is vertical. (a) SUB2, average grain width 38 μm. (b) SUP2, average grain width of 86 μm.
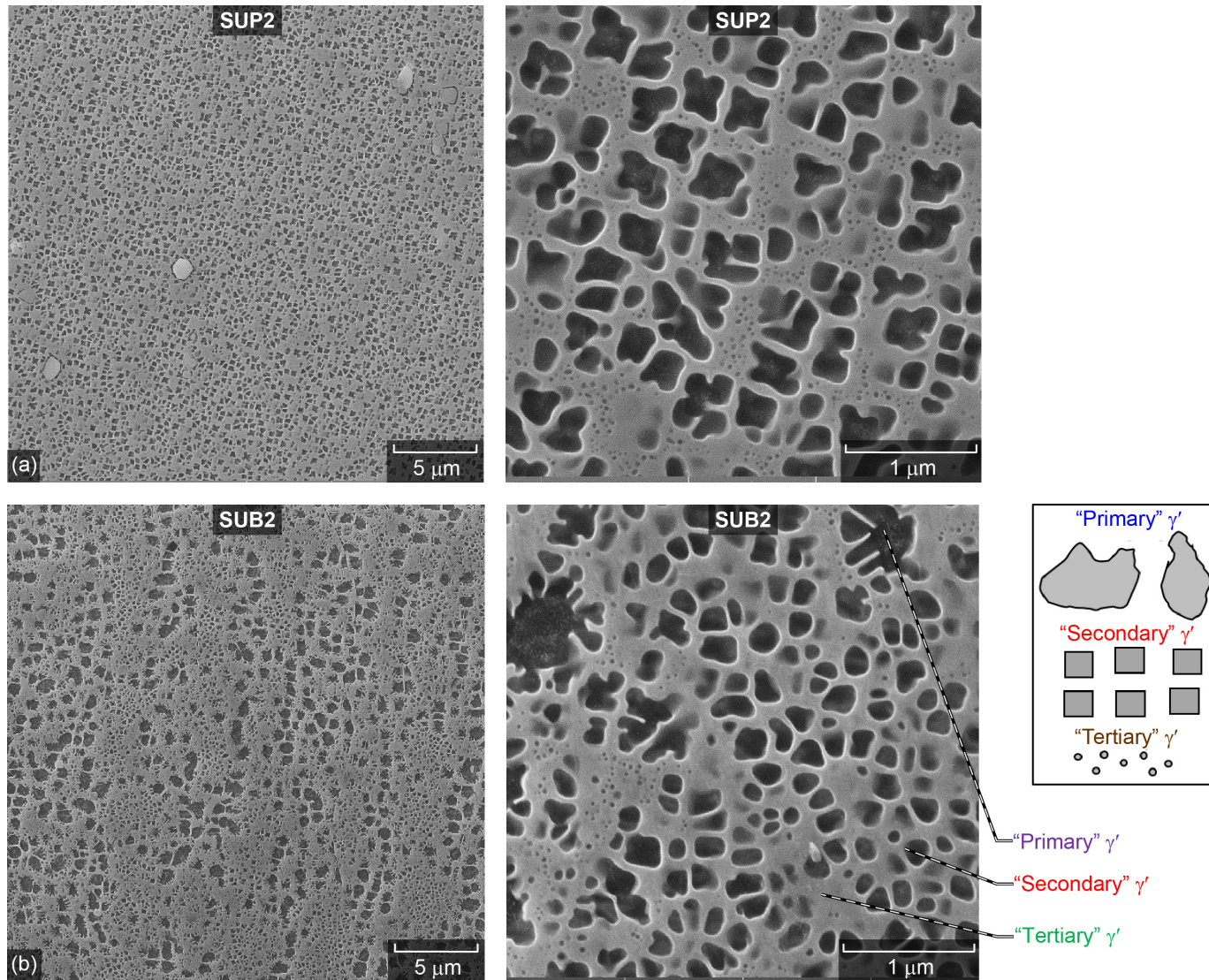
Figure 3.—Typical γ′ precipitates observed for tested materials, pointing out primary, secondary, and tertiary γ′ precipitates. Building direction is vertical. (a) SUP2. (b) SUB2.
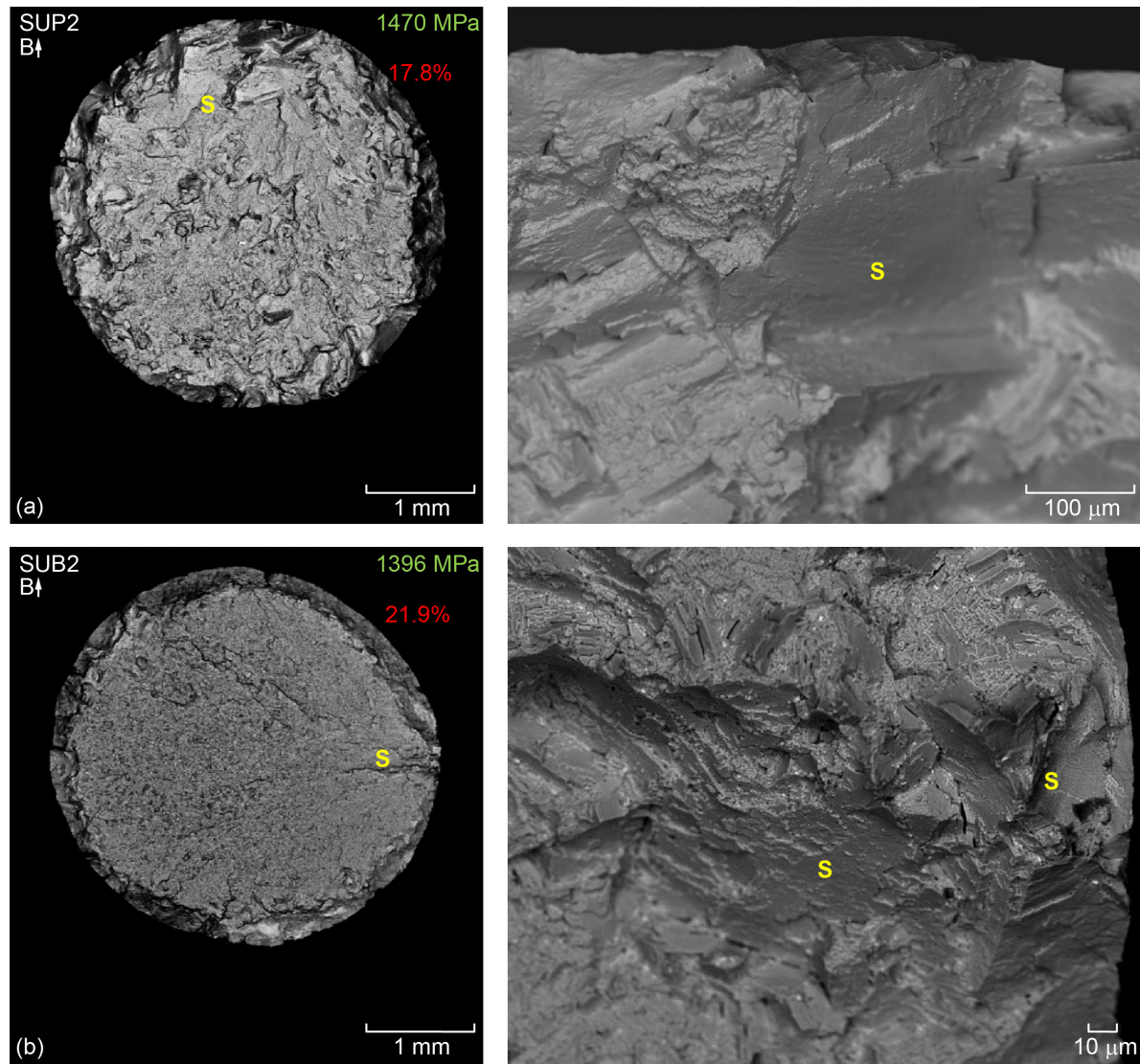
Figure 4.—Tensile fast (TF) fractures at room temperature observed for specimens loaded parallel to building direction. Ultimate tensile strength in MPa and reduction area in percentage are indicated for each specimen. (a) SUP2. (b) SUB2.
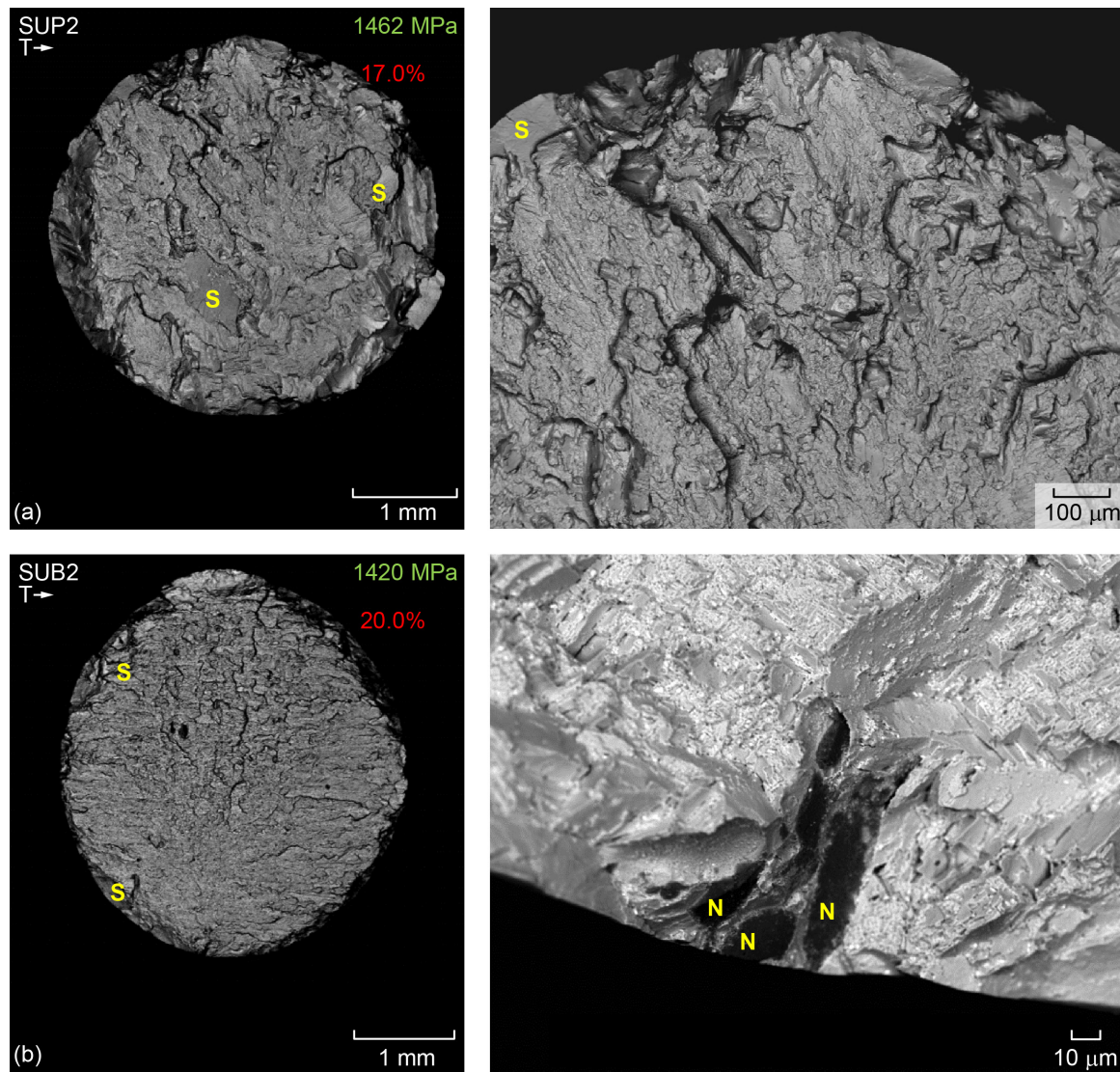
Figure 5.—Tensile fast (TF) fractures at room temperature observed for specimens loaded transverse to building direction. Ultimate tensile strength in MPa and reduction area in percentage are indicated for each specimen. Grain slip failures (S) and nonmetallic inclusions (N) are labeled. (a) SUP2. (b) SUB2.
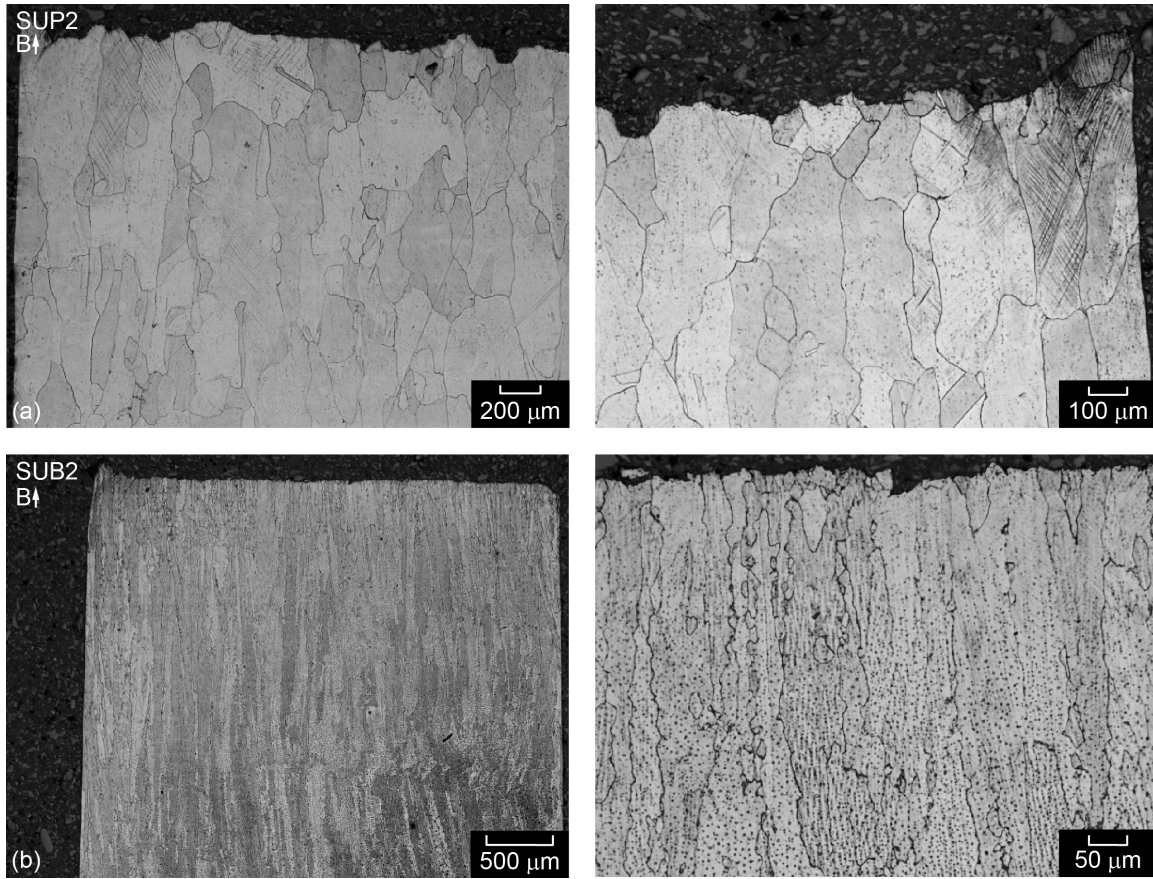
Figure 6.—Cross sections prepared parallel to vertical loading direction of tensile fast (TF) fractures at room temperature for specimens loaded parallel to building direction. No surface cracks at grain boundaries were observed. (a) SUP2. (b) SUB2.
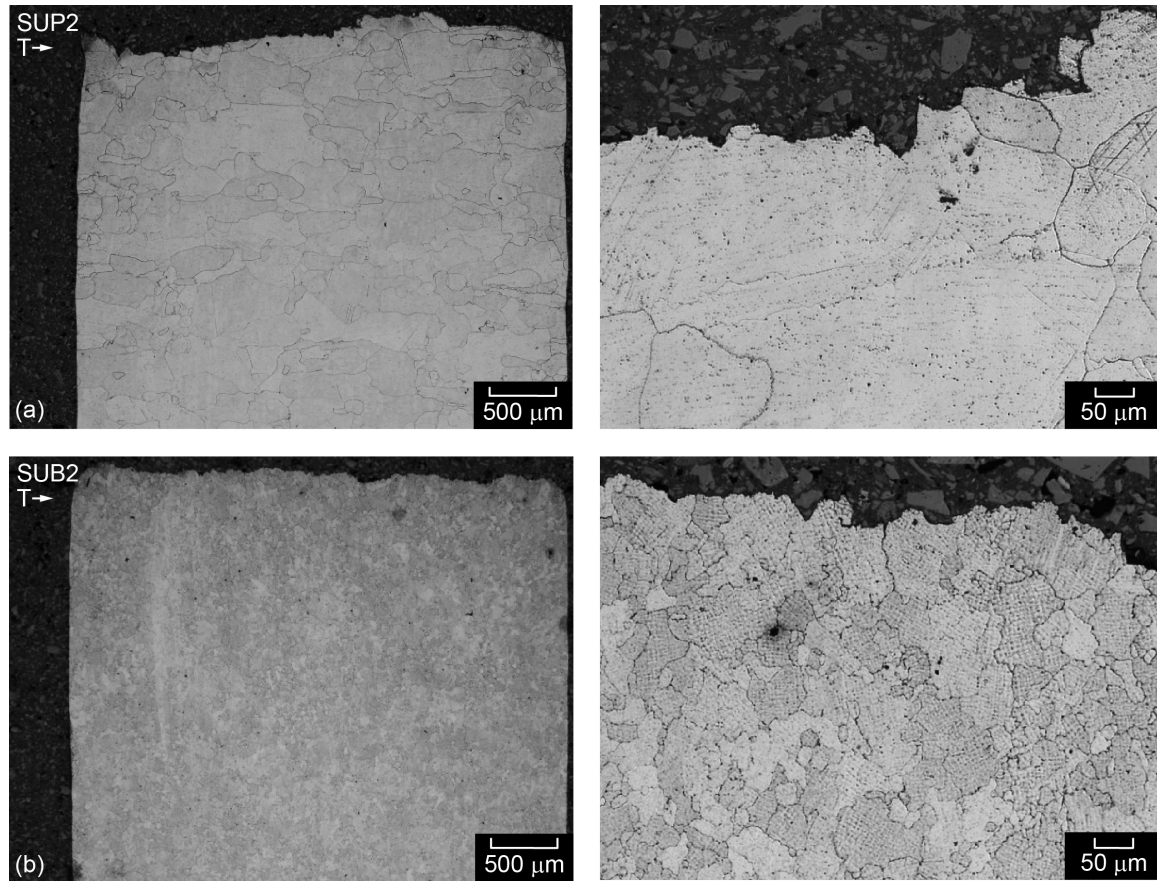
Figure 7.—Cross sections prepared parallel to vertical loading direction of tensile fast (TF) fractures at room temperature for specimens loaded transverse to building direction. No surface cracks at grain boundaries were observed. (a) SUP2. (b) SUB2.
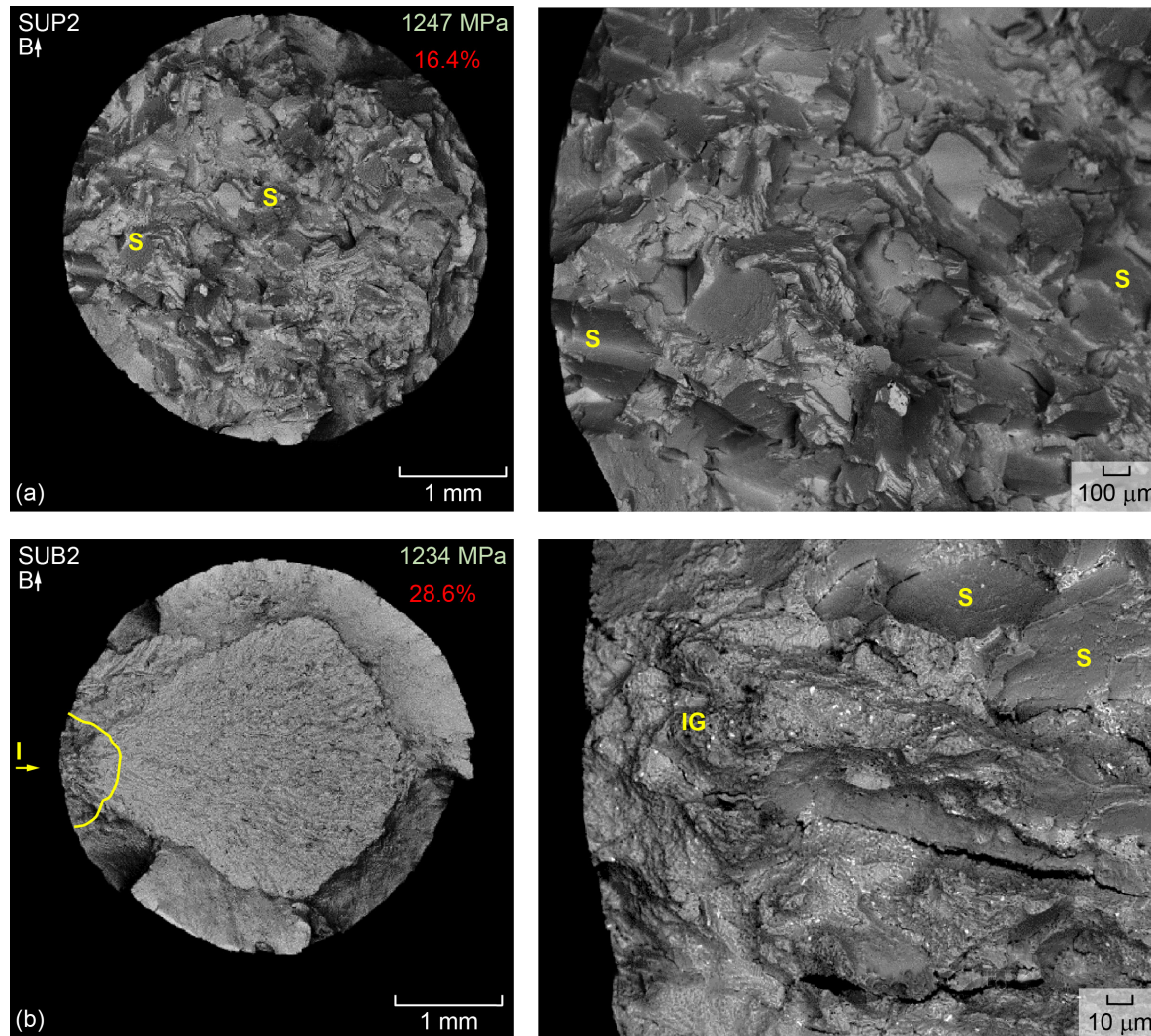
Figure 8.—Tensile fast (TF) fractures at 704 °C observed for specimens loaded parallel to building direction. Ultimate tensile strength in MPa and reduction area in percentage are indicated for each specimen. Grain slip failures (S), crack initiation points (I), and crack extent (yellow line) are pointed out. Minor intergranular (IG) failures or grains near or at exposed surface of SUB2 are also indicated. (a) SUP2. (b) SUB2.
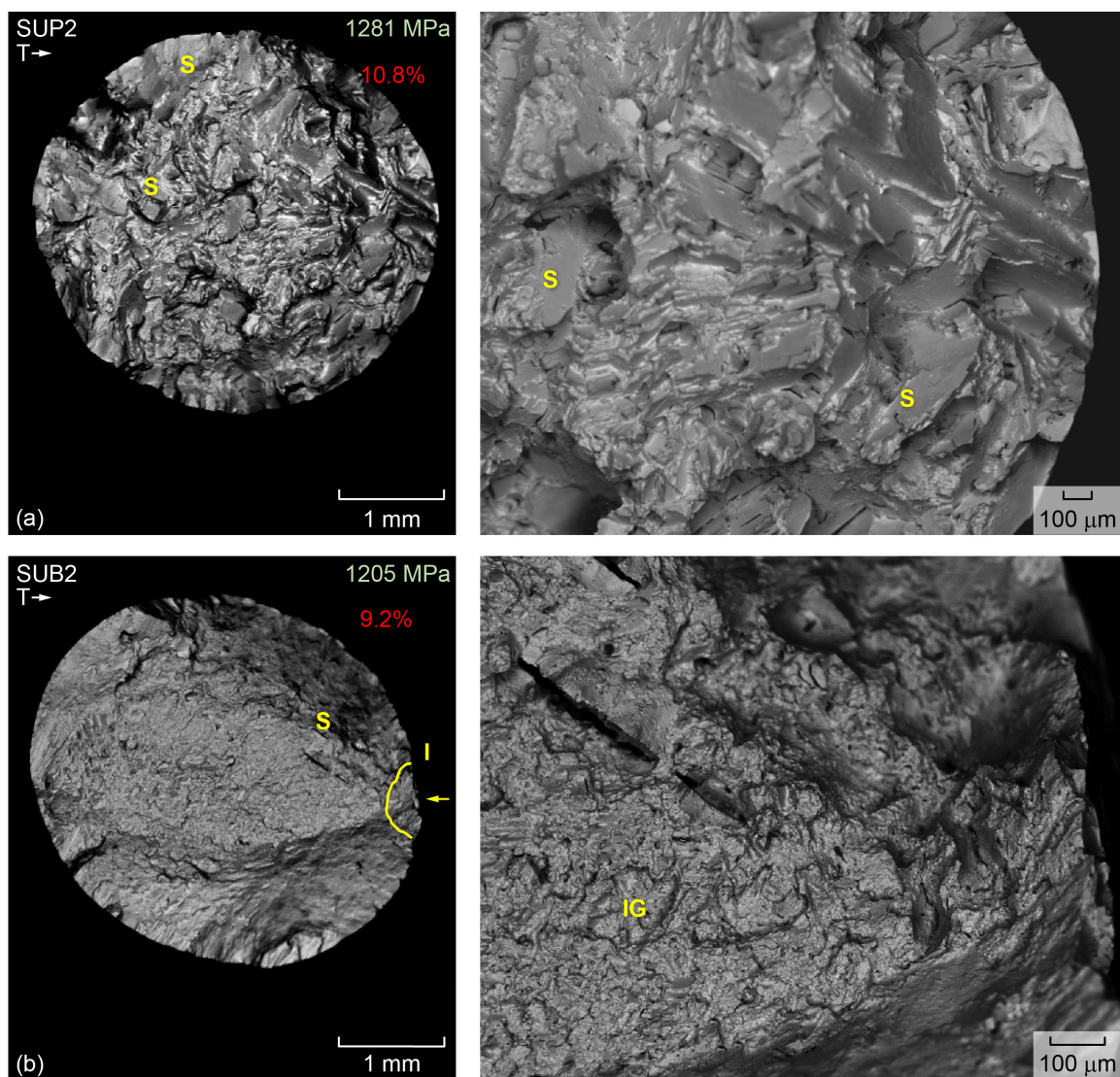
Figure 9.—Tensile fast (TF) fractures at 704 °C observed for specimens loaded transverse to building direction. Ultimate tensile strength in MPa and reduction area in percentage are indicated for each specimen. Grain slip failures (S), crack initiation points (I), and crack extent (yellow line) are identified. Minor intergranular (IG) failures of grains near exposed surface of SUB2 are also indicated. (a) SUP2. (b) SUB2.
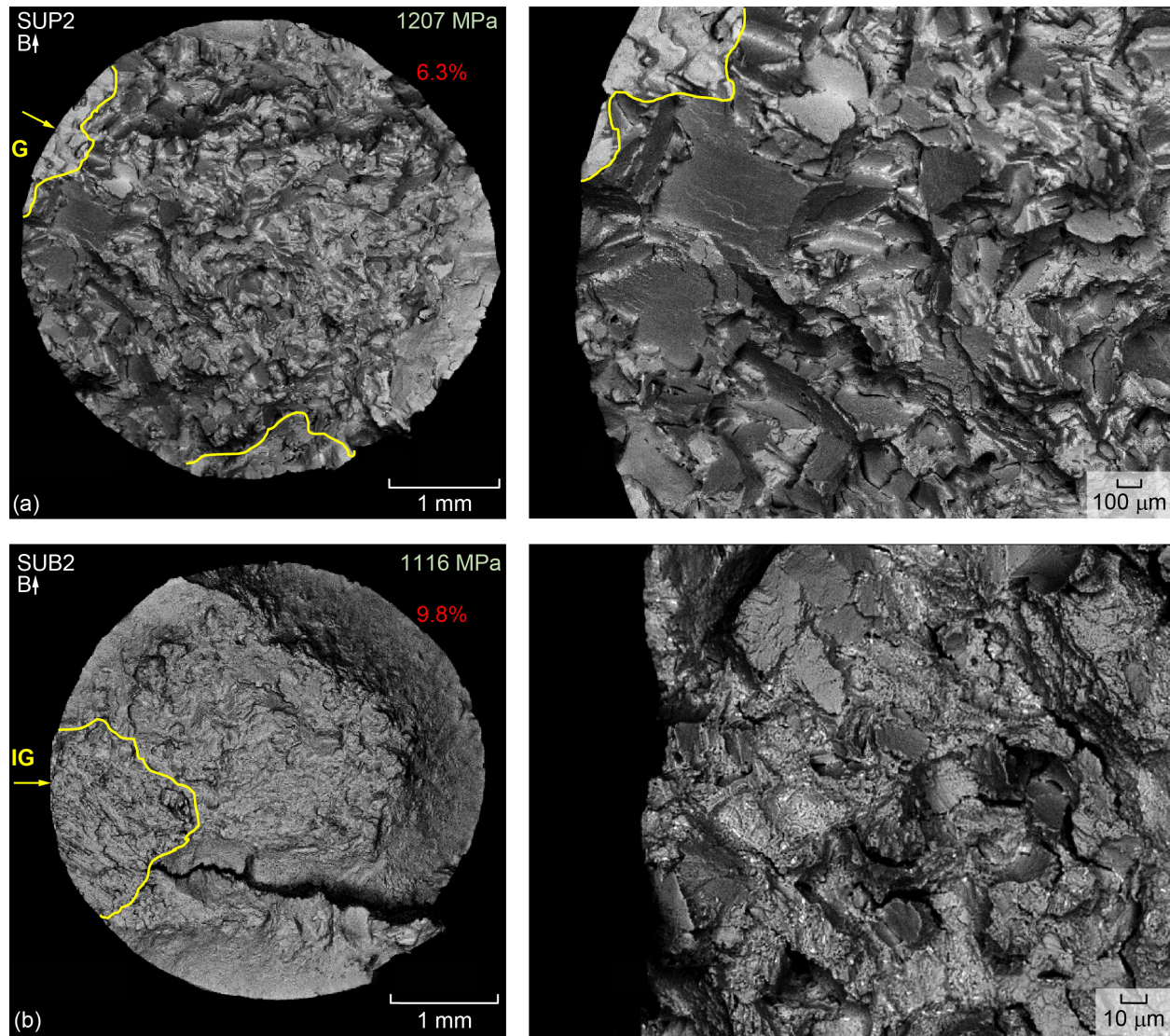
Figure 10.—Tensile slow (TS) fractures at 704 °C observed for specimens loaded parallel to building direction. Ultimate tensile strength in MPa and reduction area in percentage are indicated for each specimen. Intergranular (IG) crack initiation points and crack extents (yellow line) are identified. (a) SUP2. (b) SUB2.
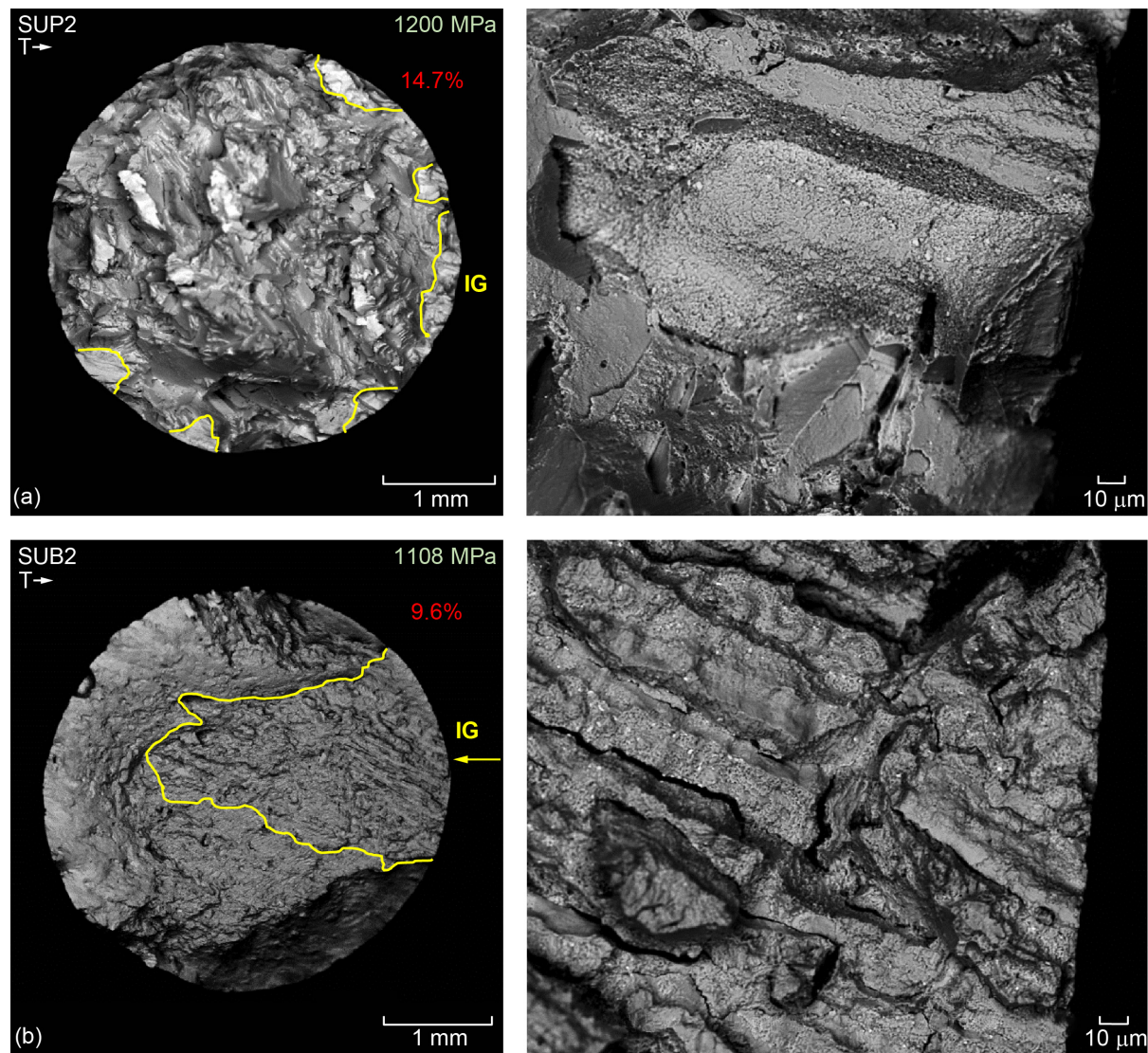
Figure 11.—Tensile slow (TS) fractures at 704 °C observed for specimens loaded transverse to building direction. Ultimate tensile strength in MPa and reduction area in percentage are indicated for each specimen. Intergranular (IG) crack initiation points and crack extents (yellow line) are identified. (a) SUP2. (b) SUB2.
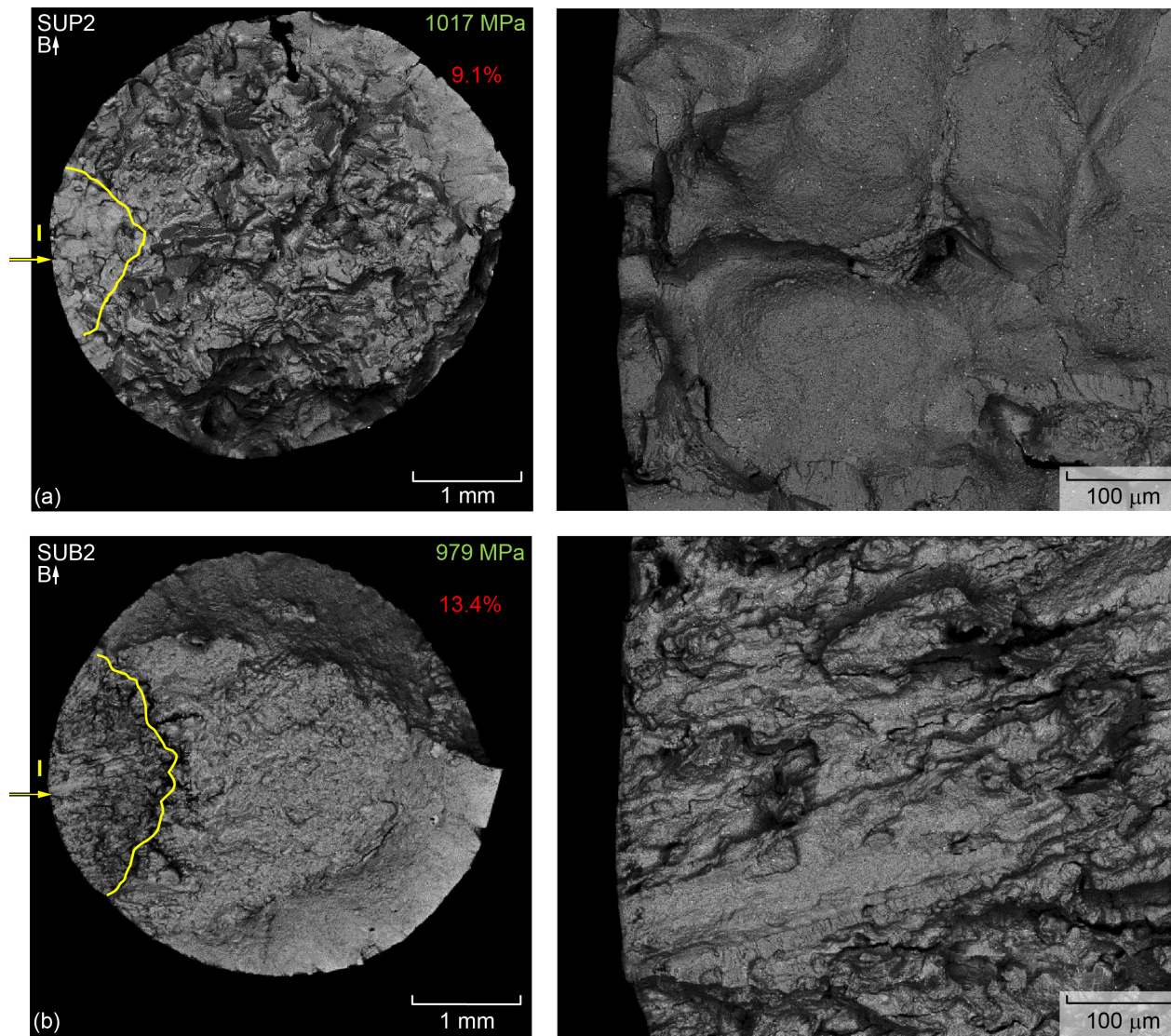
Figure 12.—Tensile slow (TS) fractures at 760 °C observed for specimens loaded parallel to building direction. Ultimate tensile strength in MPa and reduction area in percentage are indicated for each specimen. Crack initiation points (I) and crack extents (yellow line) are identified. (a) SUP2. (b) SUB2.
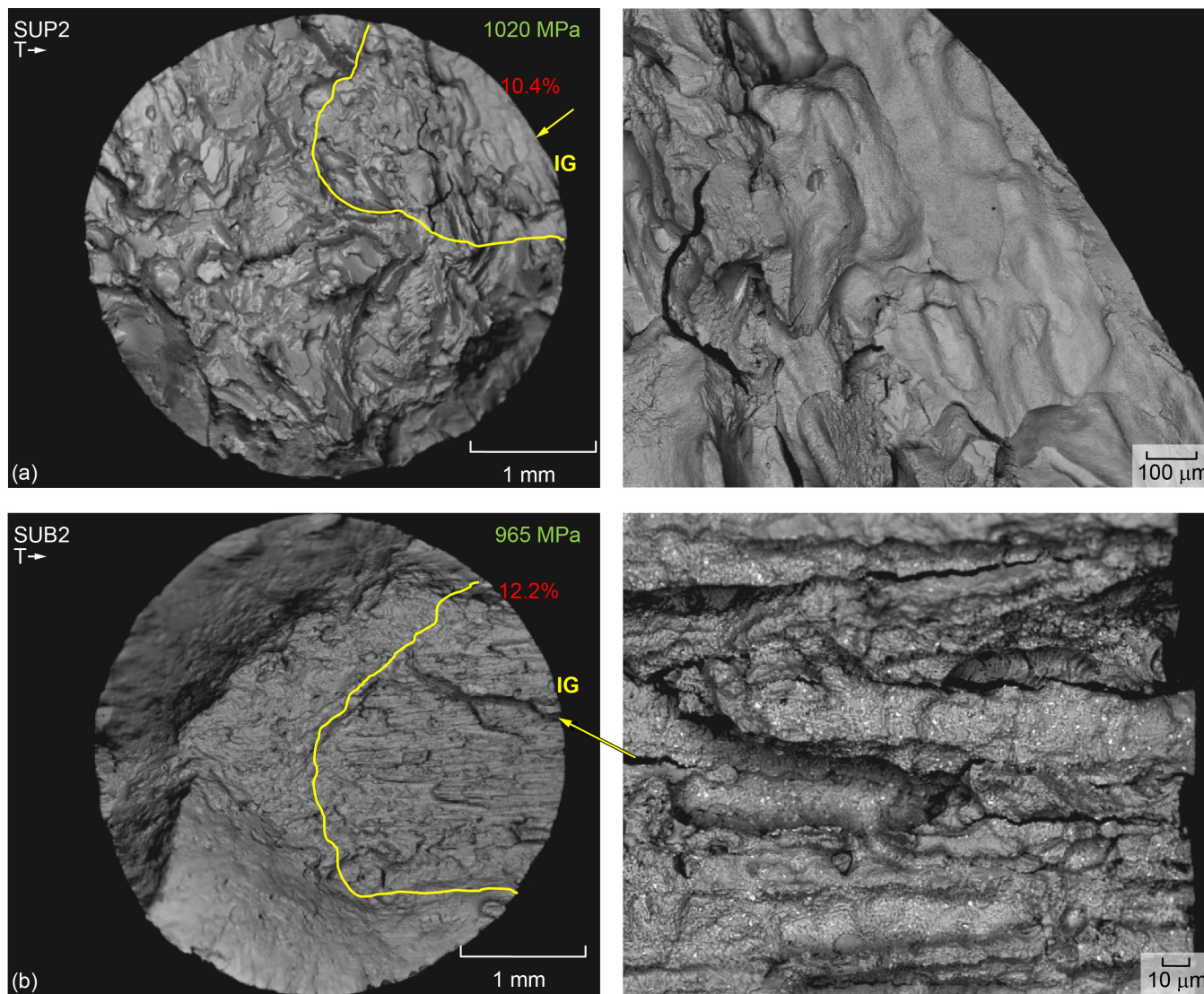
Figure 13.—Tensile slow (TS) fractures at 760 °C observed for specimens loaded transverse to building direction. Ultimate tensile strength in MPa and reduction area in percentage are indicated for each specimen. Intergranular (IG) crack initiation points and crack extents (yellow line) are pointed out. (a) SUP2. (b) SUB2.
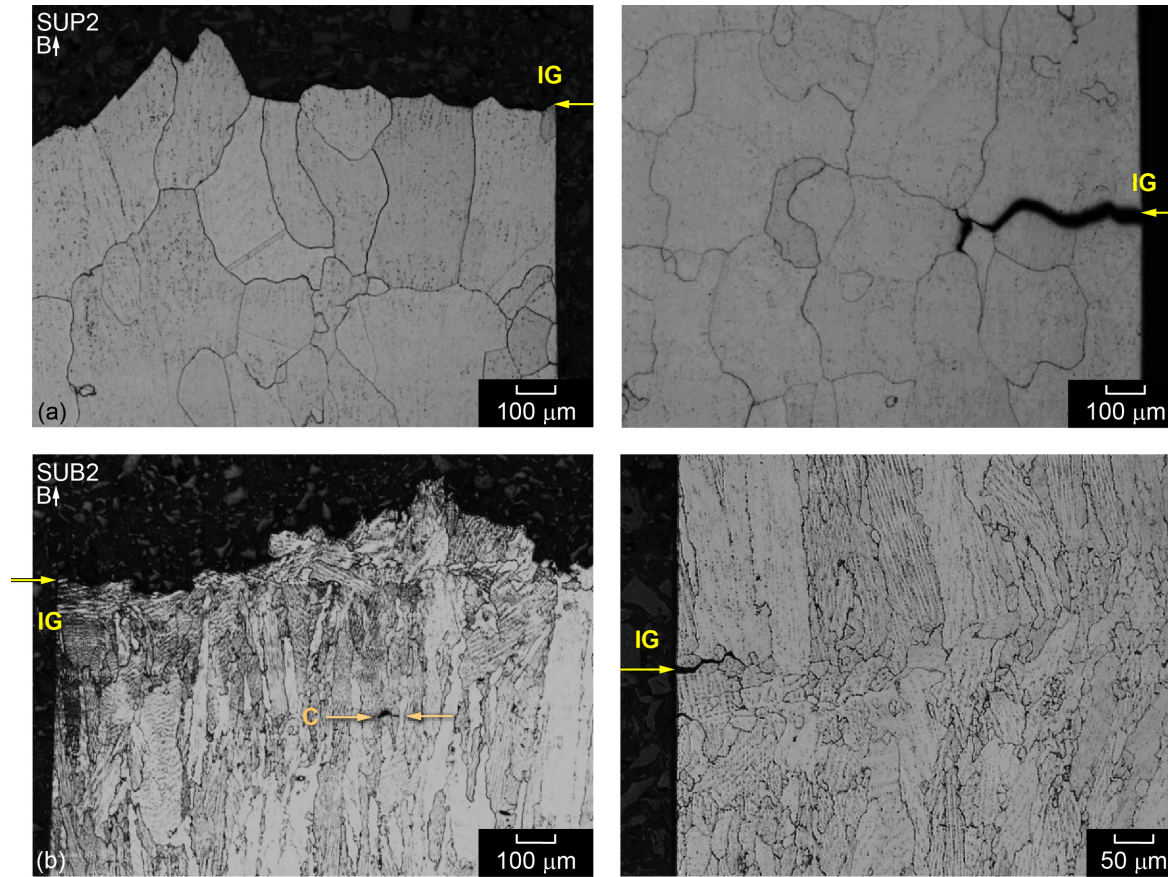
Figure 14.—Cross sections prepared parallel to vertical loading direction of tensile slow (TS) fractures at 760 °C for specimens loaded parallel to building direction. Intergranular (IG) failures and cracks are pointed out at surface, and internal cracks at fine grain colonies (C) are also indicated. (a) SUP2. (b) SUB2.
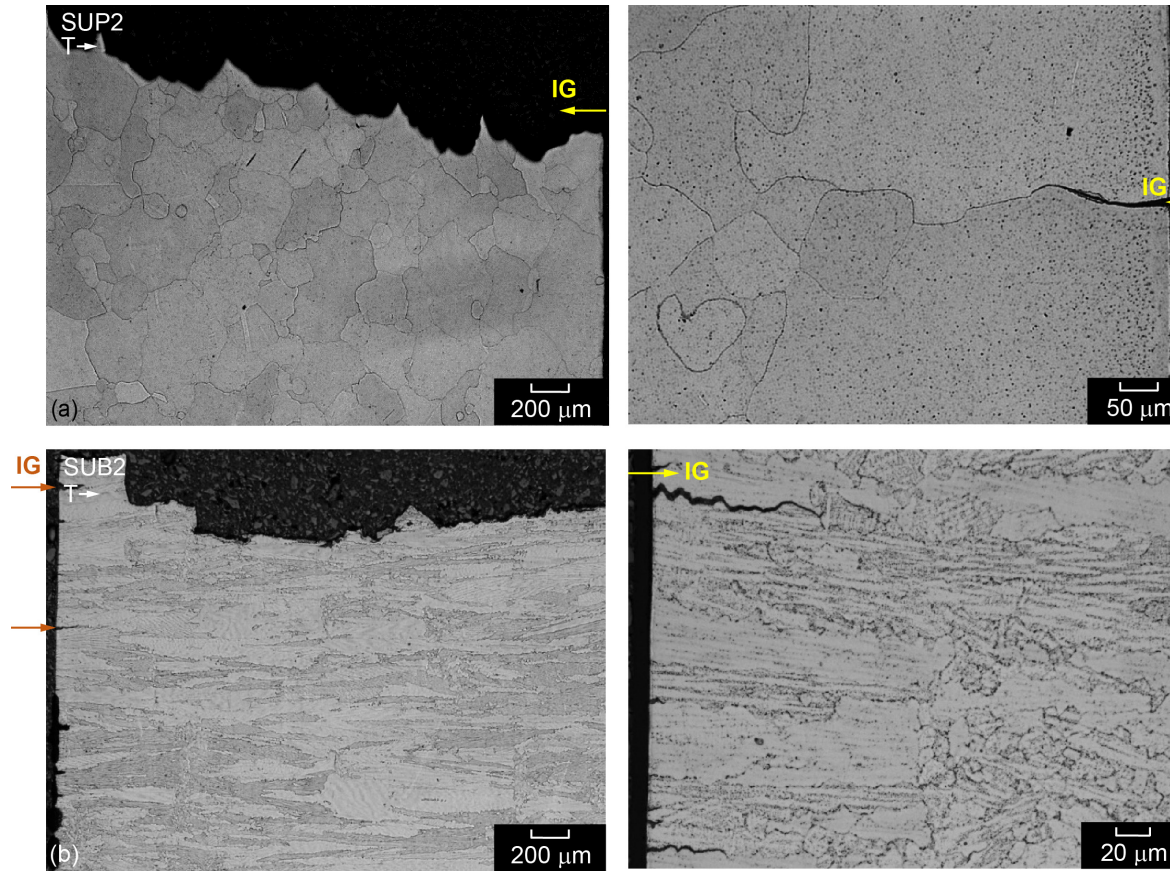
Figure 15.—Cross sections prepared parallel to vertical loading direction of tensile slow (TS) fractures at 760 °C for specimens loaded transverse to building direction. Intergranular (IG) failures and cracks are pointed out at surface, and internal cracks at fine grain colonies (C) are also indicated. (a) SUP2. (b) SUB2.
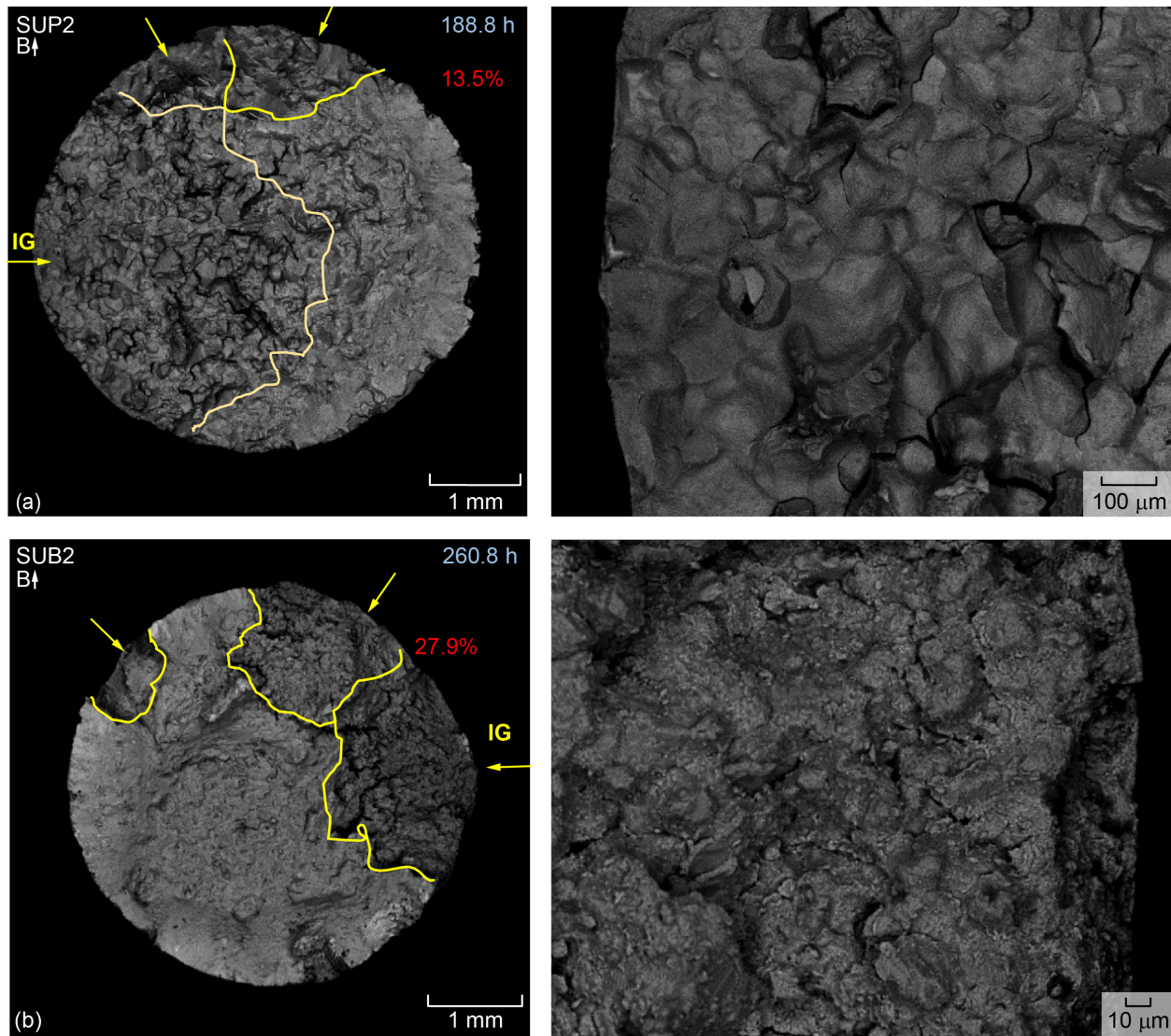
Figure 16.—Creep rupture fractures at 760 °C and 620 MPa observed for specimens loaded parallel to building direction. Rupture life in h and reduction area in percentage are indicated for each specimen. Intergranular crack initiation points (IG) and crack extents (yellow line) are pointed out. (a) SUP2. (b) SUB2.
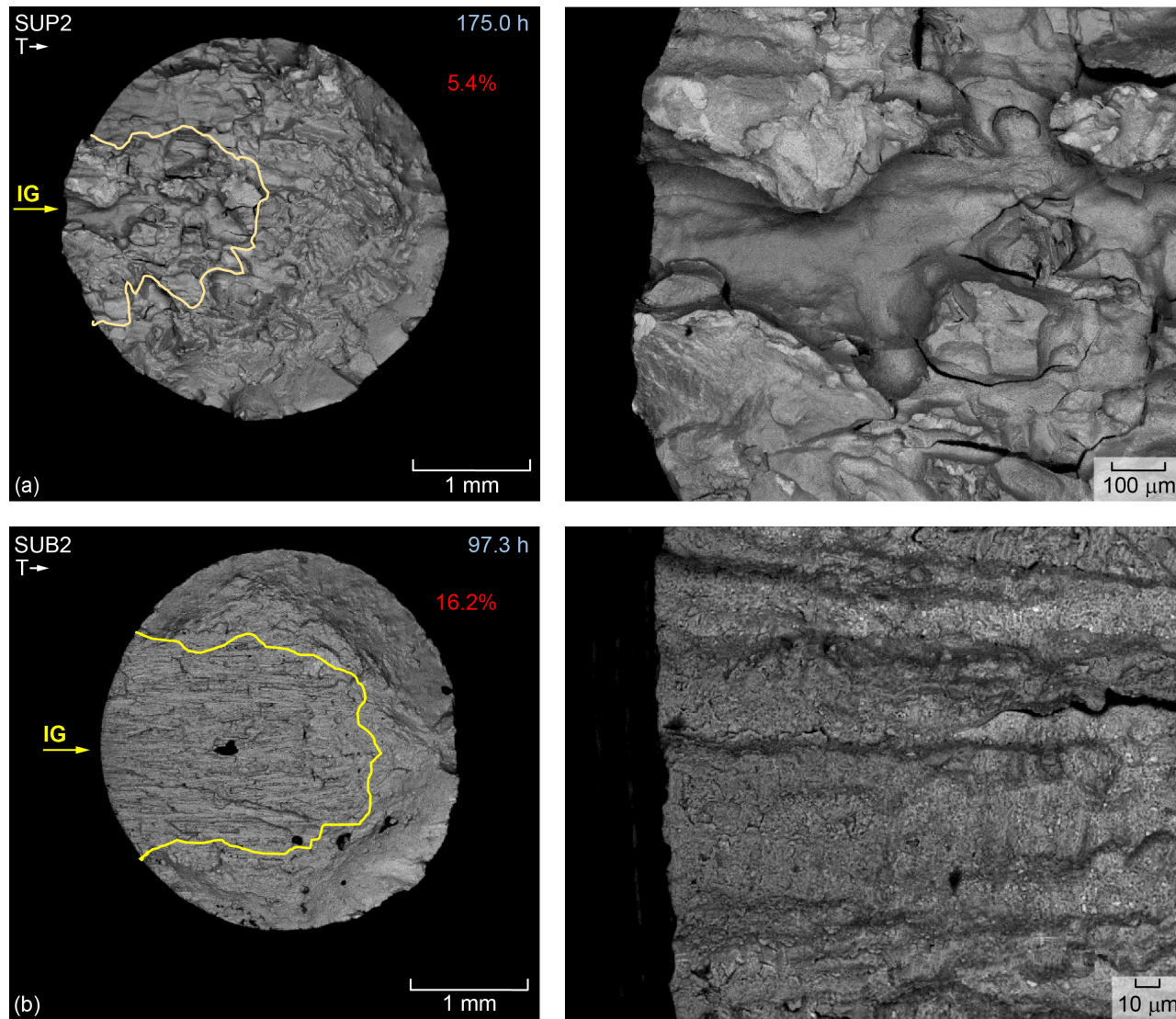
Figure 17.—Creep rupture fractures at 760 °C and 620 MPa observed for specimens loaded transverse to building direction. Rupture life in h and reduction area in percentage are indicated for each specimen. Intergranular crack initiation points (IG) and crack extents (yellow line) are pointed out. (a) SUP2. (b) SUB2.
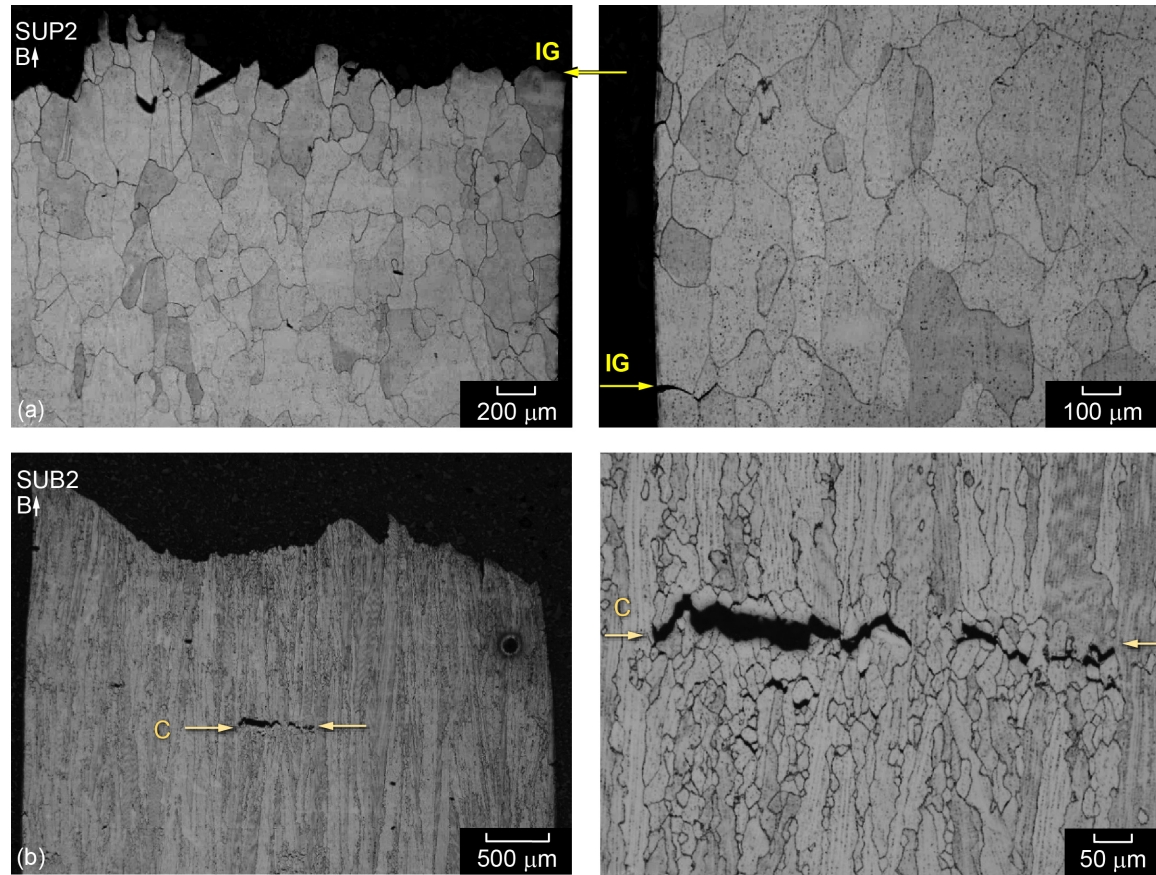
Figure 18.—Cross sections prepared parallel to vertical loading direction of creep rupture fractures at 760 °C of specimens loaded parallel to building direction. Crack initiation points (I) and intergranular (IG) failures and cracks are pointed out at surface. Internal cracks at fine grain colonies (C) are also indicated. (a) SUP2. (b) SUB2.
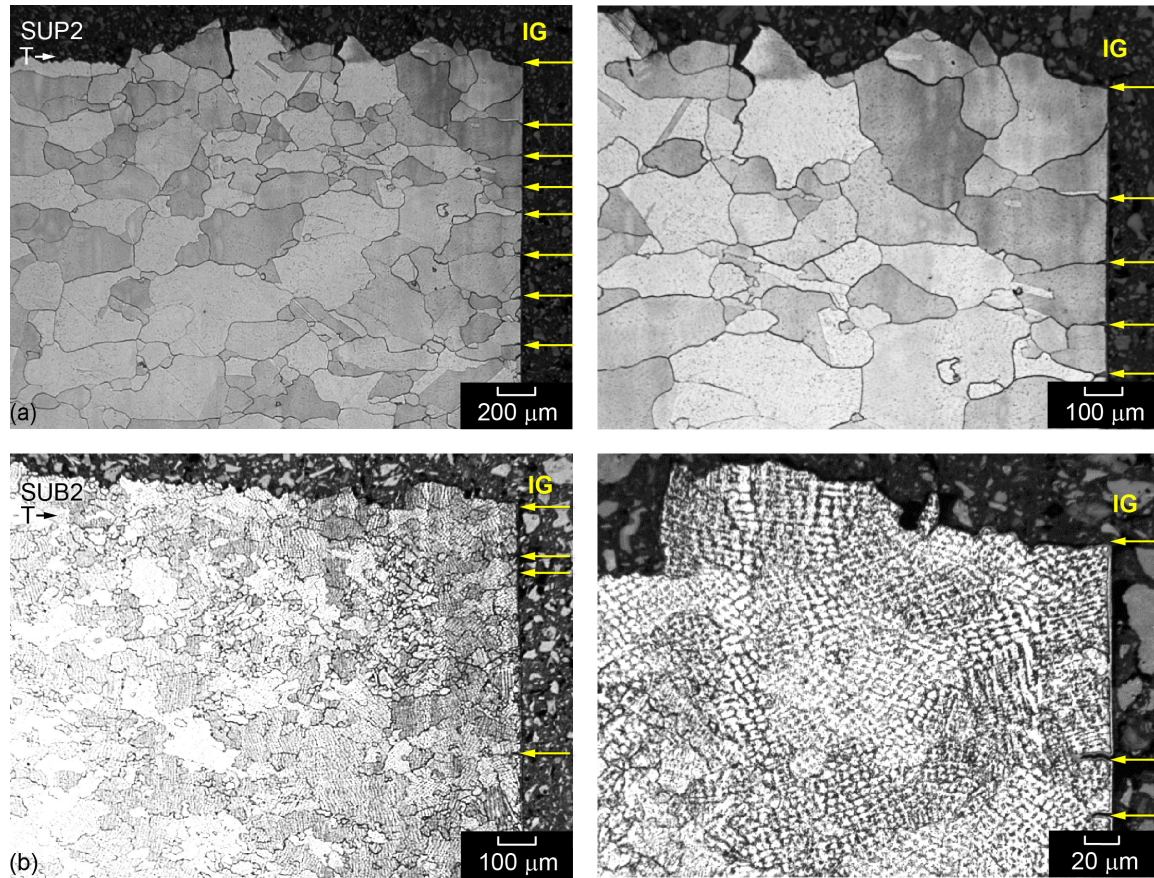
Figure 19.—Cross sections prepared parallel to vertical loading direction of creep rupture fractures at 760 °C of specimens loaded transverse to building direction. Crack initiation points (I) and intergranular (IG) failures and cracks are pointed out at surface. (a) SUP2. (b) SUB2.
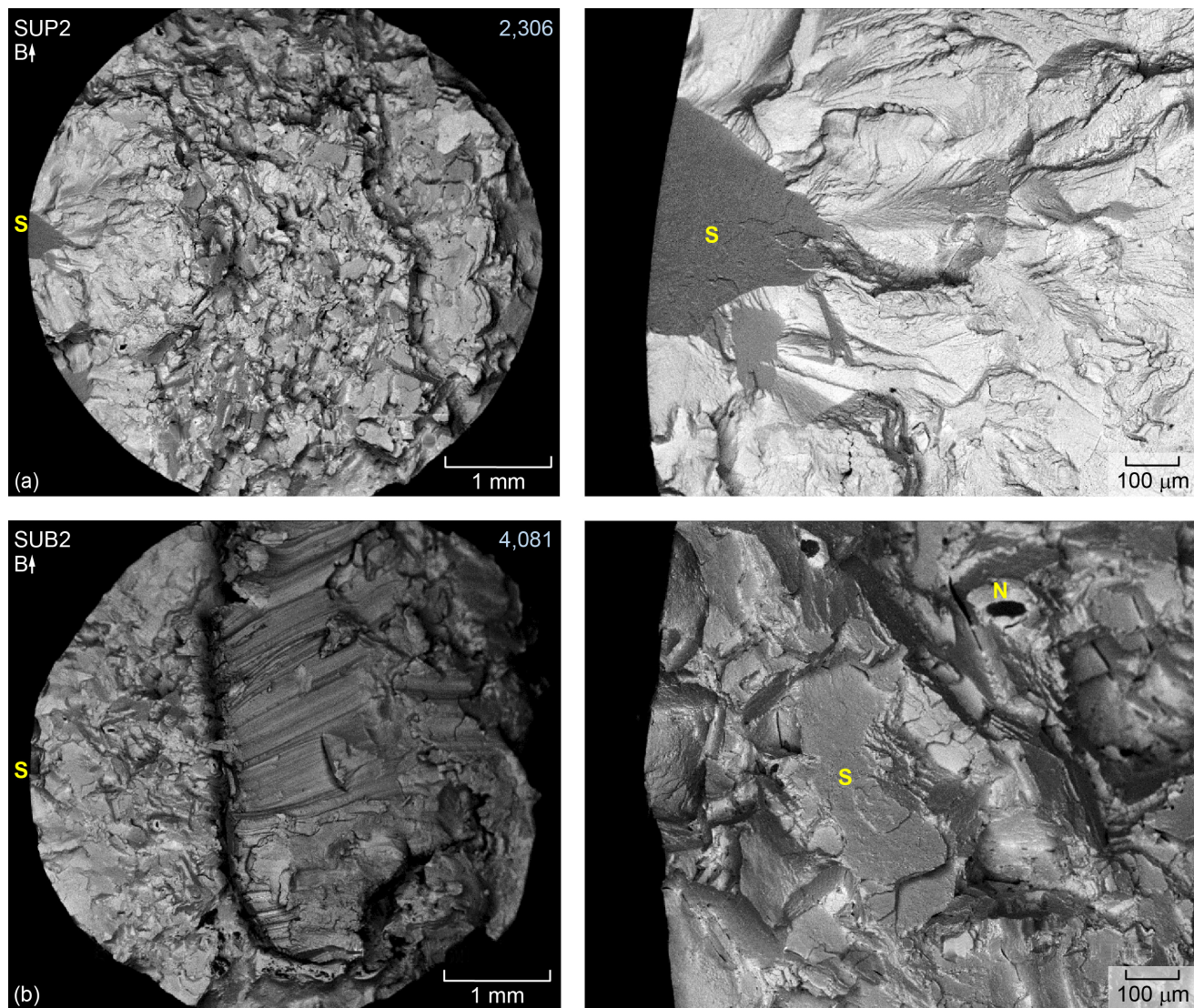
Figure 20.—Fatigue fractures at 760 °C observed for specimens loaded parallel to building direction, tested at maximum and minimum stresses near 841 and –427 MPa. Fatigue life and failure initiations at grain slip failure (S) or nonmetallic inclusions (N) are indicated for each specimen. (a) SUP2. (b) SUB2.
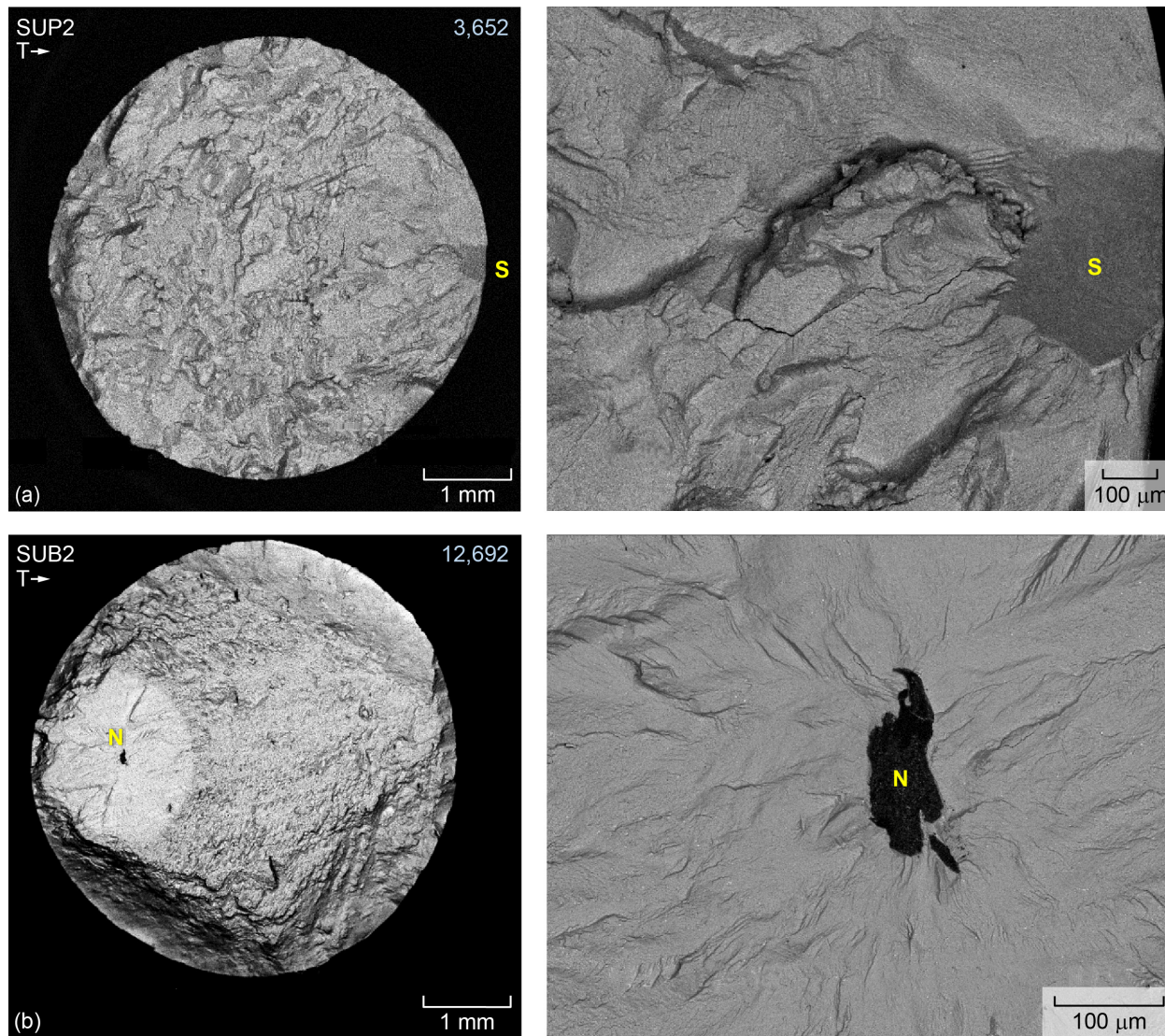
Figure 21.—Fatigue fractures at 760 °C observed for specimens loaded transverse to building direction, tested at maximum and minimum stresses near 841 and –427 MPa. Fatigue life and failure initiation at grain slip failure (S) or nonmetallic inclusion (N) are indicated for each specimen. (a) SUP2. (b) SUB2.
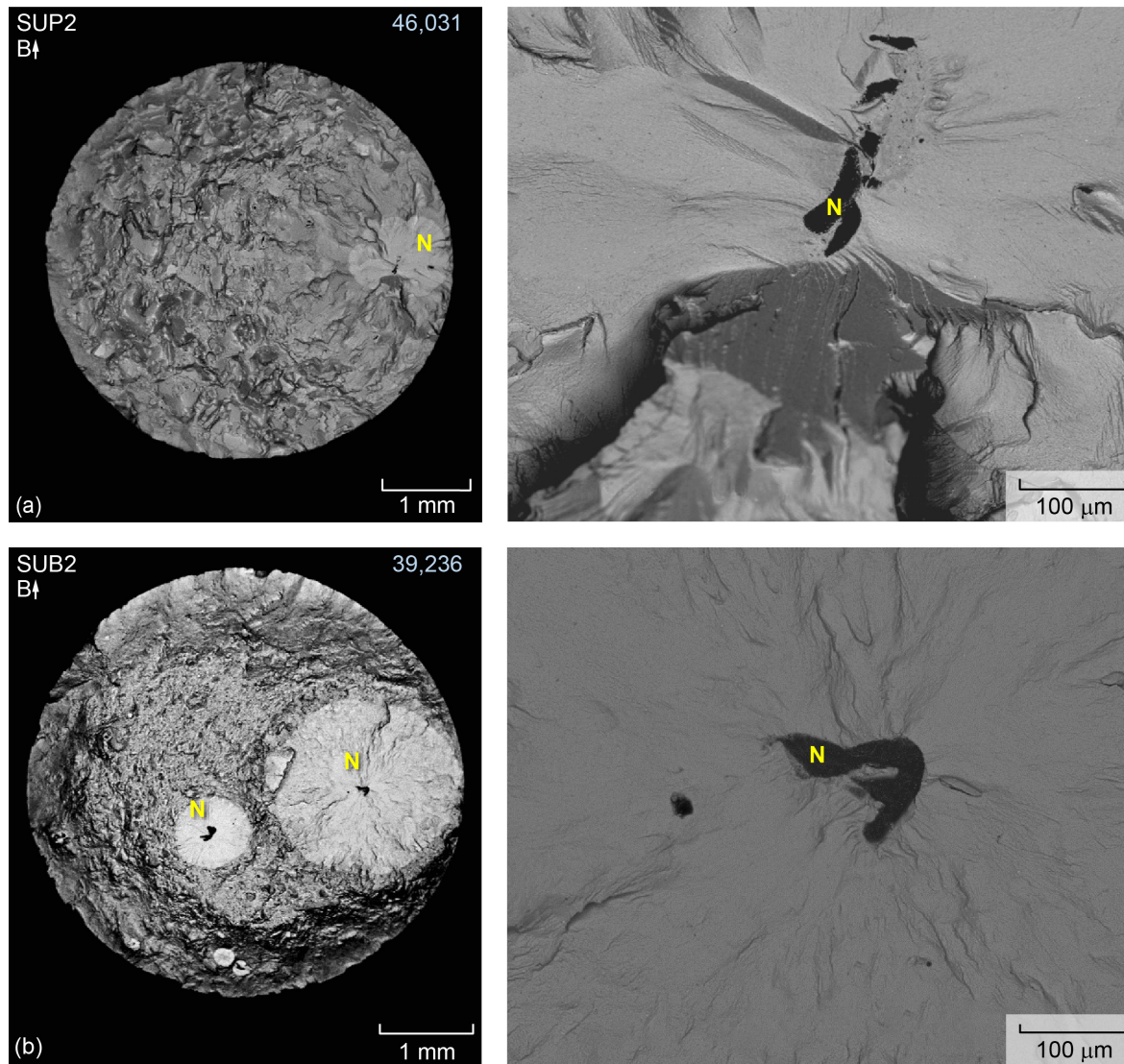
Figure 22.—Fatigue fractures at 760 °C observed for specimens loaded parallel to building direction, tested at maximum and minimum stresses of 739 and –85 MPa. Fatigue life and failure initiations at nonmetallic inclusions (N) are indicated for each specimen. (a) SUP2. (b) SUB2.
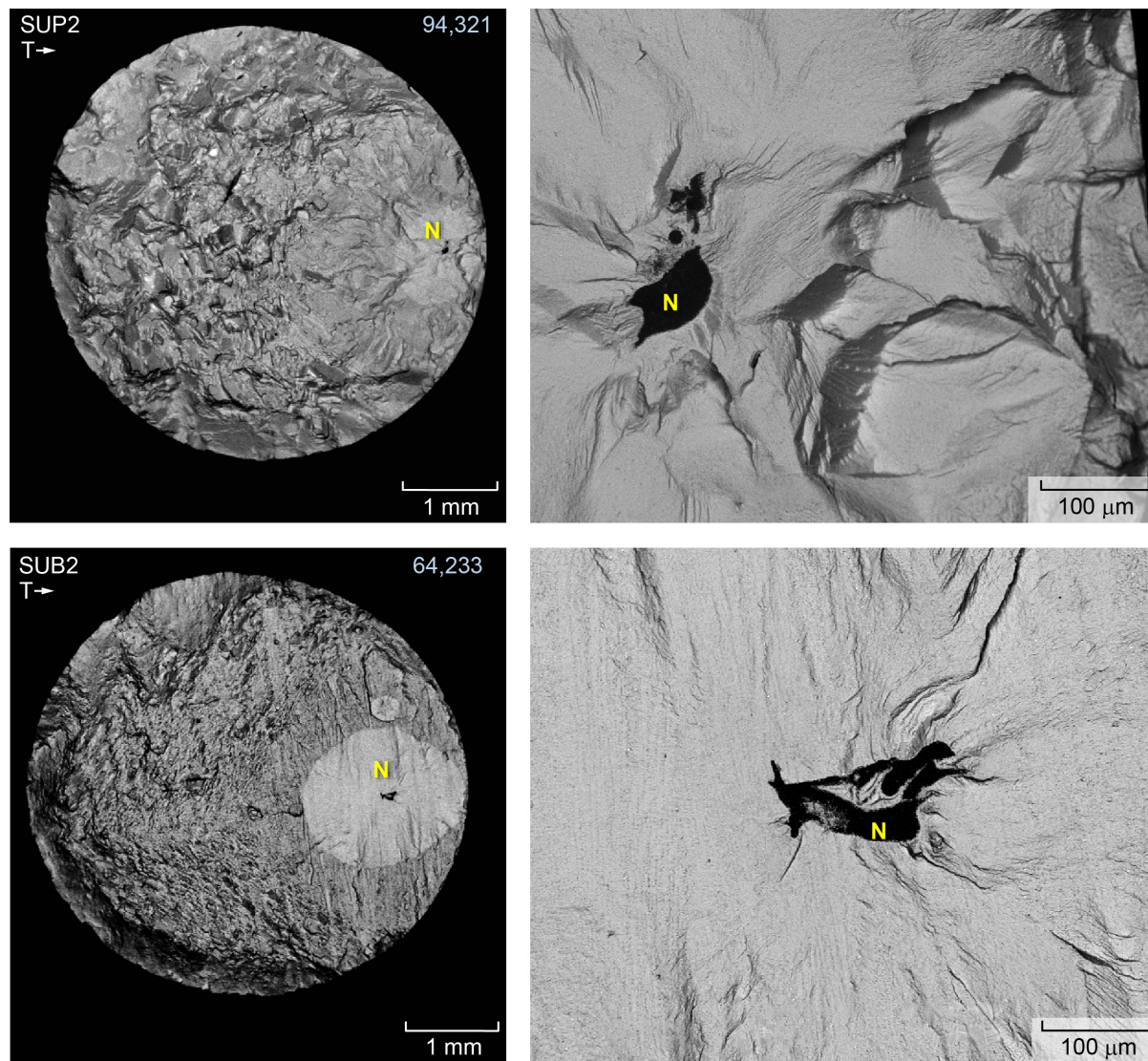
Figure 23.—Fatigue fractures at 760 °C observed for specimens loaded transverse to building direction, tested at maximum and minimum stresses of 739 and –85 MPa. Fatigue life and failure initiation at nonmetallic inclusion (N) are indicated for each specimen. (a) SUP2. (b) SUB2.